

Subthreshold ρ^0 photoproduction on ${}^3\text{He}$

M.A. Kagarlis*, Z. Papandreou, G.M. Huber, G.J. Lolos, A. Shinozaki, E.J. Brash, F. Farzanpay, M. Iurescu, and
A. Weinerman

Department of Physics, University of Regina, Regina, Saskatchewan, S4S 0A2, Canada

G. Garino[†], and K. Maruyama

Institute for Nuclear Study[‡], University of Tokyo, Tanashi, Tokyo 188, Japan

O. Konno, K. Maeda, T. Terasawa, and H. Yamazaki

Department of Physics, Tohoku University, Sendai 980, Japan

T. Emura, H. Hirosawa, K. Niwa, and H. Yamashita

Department of Applied Physics, Tokyo University of Agriculture and Technology, Koganei, Tokyo 184, Japan

S. Endo, K. Miyamoto, and Y. Sumi

Department of Physics, Hiroshima University, Higashi-Hiroshima 724, Japan

A. Leone, and R. Perrino

INFN-Sezione di Lecce, I-73100 Lecce, Italy

T. Maki

University of Occupational and Environmental Health, Kitakyushu 807, Japan

A. Sasaki

College of General Education, Akita University, Akita 010, Japan

J.C. Kim

Department of Physics, Seoul National University, Seoul 151-742, Korea

(The TAGX Collaboration)

(October 16, 2018)

A large reduction of the ρ^0 mass in the nuclear medium is reported, inferred from dipion photoproduction spectra in the 1 GeV region, for the reaction ${}^3\text{He}(\gamma, \pi^+\pi^-)\text{X}$ with a 10% duty factor tagged-photon beam and the TAGX multi-particle spectrometer. The energy range covered ($800 \leq E_\gamma \leq 1120$ MeV) lies mostly below the free ρ^0 production threshold, a region which is believed sensitive to modifications of light vector-meson properties at nuclear-matter densities. The ρ^0 masses extracted from the MC fitting of the data, $m_{\rho^0}^* = 642 \pm 40$, 669 ± 32 , and 682 ± 56 MeV/ c^2 for E_γ in the 800-880, 880-960, and 960-1040 MeV regions respectively, are independently corroborated by a measured, assumption-free, kinematical observable. This mass shift, far exceeding current mean-

field driven theoretical predictions, may be suggestive of ρ^0 decay within the range of the nucleonic field.

I. INTRODUCTION

Hadronic dynamics have until recently been comprising of two non-overlapping domains, distinctly separated along the lines of their respective description of matter as hadronic or quark. On the low-energy side of the spectrum, matter is probed on a scale where pions and baryonic resonances are the relevant constituents. These have been rather successfully employed by quasi-phenomenological models in providing prescriptions for free and in-medium hadronic interactions. At the higher-energy end, far above energies typical of baryonic resonances, quark degrees of freedom become accessible and matter tends asymptotically towards quark-gluon plasma. In this regime, described by perturbative QCD, quarks become deconfined and chiral symmetry is restored.

Although the origin of quark confinement is not known, it is evident that, whatever the reasons, it must induce spontaneous breaking of chiral symmetry [1]. The two phenomena are therefore linked and in the limit of chiral symmetry restoration, as quark masses tend to zero, vector-meson masses and widths are also expected to change [2]. The transition from hadronic to quark matter and the effect of increasing density and temperature on the properties of light vector mesons have been addressed in the context of QCD sum rules [3] as well as effective Lagrangians [4]. In particular, a temperature and density dependent lowering of the ρ^0 mass is regarded as a precursor of the chiral phase transition, expected to be measurable even at normal nuclear density [5]. Thus, the energy region from hadronic phenomenology to the domain of perturbative QCD has come to the foreground, as the study of vector-meson property modifications in this range appears to be holding the key to understanding the mechanism of chiral symmetry restoration.

The recent advent of high duty-cycle photon beams, on one hand, and high-resolution dilepton spectrometers, on the other, have opened up the possibility of reconciliation between the hadronic and quark depictions of matter. Hadronic probes coupled with hadron spectrometers had been extensively used in the past for energies up to the Δ resonance, but higher-up, where multi-pion production channels increasingly dominate, the combination becomes rapidly cumbersome due to medium distortions from initial and final state interactions. For the study of the vector mesons that couple to multi-pion states, the photon is ideally suited. The recognition of the electromagnetic interaction

as an indispensable probe at either the entrance or the exit channel, if the vector-meson field in the nuclear medium is to be delineated, has generated activity in a variety of fields.

A. Relativistic Heavy Ion Results

At relativistic energies, under extreme conditions of temperature and density, the quest for signs of a phase transition from hadronic matter to quark-gluon plasma is at the heart of experimental programs using heavy-ion beams (e.g. at CERN, GSI, and RHIC) and dilepton spectrometers. A series of pioneering studies from the CERES, HELIOS-3, and NA50 collaborations at SPS/CERN with central S + Au, S + W, Pb + Au, and Pb + Pb collisions, have largely been interpreted as indicative of a downward shift of the ρ^0 mass in the nuclear medium [6,7]. The invariant mass spectra for dilepton production that have been measured in these experiments, when compared with the respective p-A spectra, show a large enhancement at low invariant mass regions. The excess dileptons are thought to originate from the decay of mesonic resonances produced in $\pi^+\pi^-$ annihilation and, in the mass region $0.2 < m_{l+l^-} < 0.5$ GeV/c², the models advocating vector-meson medium modifications attribute the enhancement to the decay of the ρ^0 meson with a downward-shifted mass [8,9]. Nonetheless, an explanation in terms of conventional phenomenological ρ^0 -meson medium modifications is also consistent with the CERN data [10,11,12]. In this more conservative approach, the ρ^0 spectral function below 0.6 GeV/c² in dilepton invariant mass is appreciably enhanced from the contributions of “rho-sobar”-type excitations such as the ΔN^{-1} , $N^*(1720)N^{-1}$ and $\Delta^*(1905)N^{-1}$, a consequence of the strong coupling of the ρ^0 meson with $\pi^+\pi^-$ states in the nuclear medium. This being the case, the downward shift of the ρ^0 -meson mass in the nuclear medium may amount to no more than a convenient parametrization [10].

From a theoretical perspective, a model combining chiral SU(3) dynamics with vector-meson dominance in an effective Lagrangian has shown that chiral restoration does not demand a drastic reduction of vector-meson masses in the nuclear medium [13]. The latter model, in qualitative agreement with the hadronic-phenomenological models [10,12], predicts a substantial enhancement of the ρ^0 spectral density below the nominal resonance mass, with only a marginal mass reduction. This result is tantamount to the ρ^0 dissolving in the medium. Moreover, both an interpretation of the CERES data as the outcome of either medium-modified hadronic interactions, or interactions of dissociated quarks in the quark-gluon phase, yield remarkably consistent results in the framework of Ref. [13], leading to the conjecture that both the hadronic and quark-gluon phases must be present [13]. The latter conclusion is also drawn by a synthesis of the mass-scaling [5] and hadronic-phenomenological [12] models, leading to the prediction that dynamical-hadronic effects that are dominant up to about nuclear density, mainly via the highly-collective

$N^*(1520)N^{-1}$ state, gradually give way to ρ^0 -meson mass scaling as the quark degrees of freedom become increasingly relevant. In the intermediate crossover region of “duality”, both the hadronic and quark-gluon phases of matter are expected to coexist [14]. Thus, although a consensus has been reached on the issue of coexistence of the hadronic and quark-gluon phases in the transition region roughly placed upwards from ~ 1 GeV, the question remains as to the extent to which the nuclear medium induces modifications to the ρ^0 mass and width.

Other less directly related experimental conjectures of medium modifications of the ρ^0 mass have been deduced from an anomalous J/ψ suppression, reported by the NA50 collaboration for Pb + Pb collisions [15], enhanced $K^+-^{12}C$ scattering cross sections [16], and an IUCF experiment of polarized proton scattering on ^{28}Si , though in the latter the medium renormalization of the ρ^0 mass required for agreement with the data is inconsistent for different observables measured in the same experiment [17].

In summary, the experimental results discussed so far are inconclusive with regard to the magnitude of the ρ^0 -meson medium mass modification, and underline the limitations encountered in complex processes, where the probe interacts with nuclear matter via the strong interaction and the channel being investigated may not be disentangled from conventional medium effects.

B. Electromagnetic Probe Results

These difficulties are largely overcome with the use of photons which do not suffer from initial state interactions. The availability of high-flux photon beams, which have compensated for the low interaction cross sections with nuclear matter, complemented by wide-angle multi-particle spectrometers, have made possible a new generation of experiments. In the $E_\gamma \sim 1$ GeV region, matter is probed at short distances ≤ 1 fm, which is at the gateway of the energy range where vector-meson properties are expected to undergo modifications. In this domain, baryons and mesons are still the relevant constituents for the description of matter, yet their quark content becomes increasingly manifest, a fact which is reflected in QCD-inspired phenomenological models [18,19]. The ρ^0 meson is the best candidate among the light vector mesons $\rho^{0,\pm}$, ω , and φ as a probe of medium modifications, since, due to its short lifetime and decay length (1.3 fm), a large portion of ρ^0 mesons produced on nuclei will decay in the medium.

For effective measurements with the photon as probe in the 1 GeV region, kinematically complete experiments are required, which in turn necessitate the use of high-duty-cycle tagged photon beams and large-acceptance multi-particle spectrometers. These requirements were met by the TAGX detector [20] at the Institute for Nuclear Study (INS), where the TAGX collaboration has completed a series of experiments with the $^3\text{He}(\gamma, \pi^+ \pi^-)X$ reaction and

a 10% duty-cycle tagged photon beam. First, a lower-energy experiment ($380 \leq E_\gamma \leq 700$ MeV) measured the single- and double- Δ contributions to $\pi^+\pi^-$ production [21]. Having established these important non- ρ^0 dipion processes, the kinematics of the ${}^3\text{He}(\gamma, \pi^+\pi^-)\text{X}$ reaction were investigated in the range $800 \leq E_\gamma \leq 1120$ MeV, aiming at the $\rho^0 \rightarrow \pi^+\pi^-$ channel.

Both the coherent and quasifree ρ^0 photoproduction mechanisms are relevant in the energy region of interest. For a ${}^3\text{He}$ target, the energy threshold for the former is $E_\gamma \approx 873$ MeV, whereas the 1.083 GeV energy threshold of the elementary ρ^0 photoproduction reaction on a nucleon is lowered for the quasifree channel in the nuclear medium, as the Fermi momentum of the struck nucleon may be utilized to bring the ρ^0 meson on shell. Coherent photoproduction on nuclei is characterized by small four-momentum transfers, resulting in ρ^0 mesons which mostly decay outside of the nucleus [22]. The latter is, consequently, of limited utility in probing vector-meson medium modifications.

In contrast, quasifree subthreshold photoproduction ($E_\gamma < 1.083$ GeV) on one hand warrants that the interaction took place in the interior of the nucleus, since the nucleon Fermi momentum is required to produce the ρ^0 , and on the other produces slower ρ^0 mesons, more likely to also decay inside the nucleus. Moreover, subthreshold photoproduction, whether the target nucleus remains bound in the final state (exclusive channel) or decomposes to its constituent nucleons (breakup channel), may be correlated with either a nuclear mean-field or nucleonic medium effect on vector-meson properties (Section VB). Specifically, exclusive subthreshold photoproduction produces ρ^0 mesons which, on the average, traverse distances comparable to the size of the nucleus before their hadronic decay. This process is therefore a probe of vector-meson medium modifications at normal nuclear densities, a regime which has been the focus of mean-field driven theoretical models. The breakup channel, on the other hand, is more likely to produce ρ^0 's which are slower relative to the struck nucleon and may travel distances shorter than the nucleonic radius before decaying (Section VB). Thus, large densities in the interior of the nucleus may become accessible via the breakup channel, amounting to a nucleonic medium effect. This is the realm of the emerging hadronic-quark nature of matter, a domain virtually unexplored. In the deep subthreshold region, and for large momentum transfers to the target nucleus, the coherent and exclusive-quasifree channels are suppressed, and the breakup-quasifree process becomes dominant. It is the subthreshold dynamics that motivated the $800 \leq E_\gamma \leq 1120$ MeV ρ^0 photoproduction experiment.

The aim of the experiment being as stated above, the choice of ${}^3\text{He}$ as the target becomes almost ideal. The low photon energies utilized to induce subthreshold photoproduction result in slow ρ^0 mesons with a small Lorentz boost, and therefore a large probability for decay within the nuclear volume. Thus, in the case of the exclusive channel,

a large nuclear radius is not necessary, and the larger nuclear density of a heavier target is predicted to have only a marginally enhanced effect on the ρ^0 meson mass [19]. Furthermore, if the breakup process is dominated by the nucleonic field, the size of the target nucleus is irrelevant. Finally, the ${}^3\text{He}$ target is the lightest nucleus where a nuclear medium effect may be discernible, without the complexity of overwhelming final state interactions (FSI).

The ρ^0 detection is further aided by the inherent selectivity of the TAGX spectrometer (Section II B) to coplanar $\pi^+\pi^-$ processes [20]. This is due to the limited out-of-plane acceptance of the spectrometer, which preferentially selects the $\rho^0 \rightarrow \pi^+\pi^-$ channel, at the expense of two-step processes (e.g. FSI) and uncorrelated $\pi^+\pi^-$ production at distinct reaction vertices, the latter accounting for the majority of non- ρ^0 background events (Section IV A). This favorable feature of the spectrometer promotes an otherwise small component of the total amplitude, namely the subthreshold breakup channel, to a sizeable experimental signal.

The mass of the ρ^0 meson in the nuclear medium was extracted from the dipion spectra of the $800 \leq E_\gamma \leq 1120$ MeV experiment with the aid of Monte Carlo (MC) simulations [23]. The reported mass shift was far larger than the predictions of any mean-field driven model pertaining to the exclusive process for ${}^3\text{He}$ [19]; a calculation based on QHD assuming a deep scalar potential yielding a ρ^0 - ${}^3\text{He}$ bound state, on the other hand, produced much better agreement [24]. The result of Ref. [23] led to a reanalysis of the lower-energy measurements [21] including the $\rho^0 \rightarrow \pi^+\pi^-$ channel, and allowing for ρ^0 production with a shifted mass. The outcome of this reanalysis was an even larger shift [25], possibly indicating a mechanism other than those previously considered. A nucleonic medium effect, as sketched earlier, may be consistent with a large ρ^0 -mass reduction, although a theoretical model has yet to be fully developed [26,27]. Though more work is needed to firmly establish and better understand these results [28], the ${}^3\text{He}(\gamma, \pi^+\pi^-)X$ experiment for photon energies in the range $800 \leq E_\gamma \leq 1120$ MeV constitutes the first direct measurement of the ρ^0 mass in the nuclear medium. In this report, a new and more thorough analysis is presented, including the first direct evidence of the characteristic $J = 1$ signature of the ρ^0 meson decay in the subthreshold region, as well as refinements in the simulations and fitting procedure, relative to the analysis of Refs. [21,23,25], leading to higher confidence in the extraction of the in-medium ρ^0 mass.

The paper is organized in six sections. In Section II, the experimental set-up and the calibration procedure are reviewed. In Section III the data-analysis algorithm is outlined in conjunction with the experimental aspects of Section II. Section IV focuses on the MC techniques and the fitting of the data, leading to the extraction of the mass shift. In Section V the data are compared with the MC calculations, and the ρ^0 mass shifts are discussed. Finally, the conclusions are presented in Section VI.

II. APPARATUS

The INS tagged photon beam and the TAGX spectrometer (Fig. 1) [20], the new straw drift chamber [29], and different aspects of the data-analysis procedure [20,21] have all been described in detail elsewhere, where the reader is referred for a more extensive discussion. In this section, a brief overview of the experimental apparatus is provided, as it applies for the ${}^3\text{He}(\gamma,\pi^+\pi^-)\text{X}$ measurements, stressing the elements that were either introduced for the first time in this experiment, or that are important for the data analysis.

A. Photon beam and ${}^3\text{He}$ target

The photon beam is produced utilizing the 1.3 GeV Tokyo Electron Synchrotron. A series of innovative technical improvements led in 1987 to the upgrading of the photon beam to one of medium duty cycle. In the present experiment, the endpoint electron energy E_s is 1.22 GeV at an average 10% duty factor, corresponding to a 5 ms extraction time. The instantaneous energy of the extracted electrons has a sinusoidal dependence, and it is known by measuring the extraction time. The extracted electrons are directed via a beamline onto a thin platinum radiator where bremsstrahlung photons are produced, while the scattered electrons are bent away from the beam by a rectangular analyzer magnet of 1.17 T. The magnet settings of the extraction beamline vary sinusoidally in time, in phase with the E_s energy. An array of 32 scintillator electron-tagging counters, each with a 10 MeV/c momentum acceptance, detect the scattered electrons. The position of the tagger registering the scattered electron determines its energy, and consequently that of the bremsstrahlung photon as $E_\gamma = E_e - E_{e'}$ with $\Delta E_\gamma \sim \pm 5$ MeV accuracy. A second set of 8 backing taggers participates in the coincidence triggering signal, along with the 32 frontal ones, and is discussed in the following section. The tagged photon intensity was maintained at an average of $\sim 3.5 \times 10^5$ γ/s , well within the tolerance of the data acquisition system for accidental triggers. The photons, distributed over a beam spot of ~ 2 cm in diameter, are subsequently incident on a liquid ${}^3\text{He}$ target. The target is at a temperature of 1.986 ± 0.001 K, corresponding to a 0.0786 g/cm³ density, and is contained in a cylindrical vessel 90 mm in height and 50 mm in diameter at the center of the TAGX spectrometer [30].

The tagger hits are related to the photon flux incident upon the target after efficiency corrections. In particular, due to the collimation of the photon beam downstream from the taggers, some of the tagged photons do not reach the target. To determine the tagging efficiency, and consequently the photon flux, a lead-glass Čerenkov counter is placed in the photon beam, with reduced flux, downstream from the target and the tagger scalers are periodically

recorded both with and without the platinum radiator in place. The efficiency per tagger counter is determined by the relation

$$\eta_{i \in [1,32]} = \frac{[\check{C} \cdot T_i]_{in} - [\check{C} \cdot T_i]_{out} - [\check{C}_{acc} \cdot T_i]_{in}}{T_{i_{in}} - T_{i_{out}}} \quad (1)$$

where T_i is the scaler count for each of the frontal taggers. The term $[\check{C} \cdot T_i]_{out}$ corresponds to the coincidences between a tagger-counter and a lead-glass Čerenkov hit from a spurious photon not originating from the platinum radiator, and $[\check{C}_{acc} \cdot T_i]_{in}$ is the number of accidental coincidences with the radiator in place, but with the Čerenkov hit registering with a delay of the order of 100 ns with respect to the tagger counter signal. These two terms turn out to be negligible relative to the term $[\check{C} \cdot T_i]_{in}$ in Eq. (1), which gives the efficiency-corrected number of tagged photons per tagger reaching the target as

$$N_{i \in [1,32]} = \eta_i T_{i_{in}} \left(1 - \frac{T_{i_{out}}}{T_{i_{in}}} \right). \quad (2)$$

The efficiencies η_i and radiator out/in ratios $\mathcal{R}_i = T_{i_{out}}/T_{i_{in}}$ for the 32 frontal taggers are recorded in a number of dedicated runs, in regular intervals throughout the experiment, and they are used, along with Eq. (2), in the empty-target background subtraction procedure applied to the measured spectra (see Section III).

B. Spectrometer

The TAGX spectrometer has an acceptance of π sr for charged particles (neutral-particle detection was not utilized in the present experiment), and has been in use at INS since 1987. It consists of several layers of detector elements (Fig. 1) positioned radially outwards from the target vessel, which is located at the center of the 0.5 T field of a dipole analyzer magnet.

Directly surrounding the target container is the inner hodoscope (IH), made up of two sets of six scintillator counters, one on each side of the beam. The IH is used in the trigger, as well as in measuring the time of flight (TOF) of the outgoing particles [20,29]. As it is placed inside a strong magnetic field, the light signal is carried by optical fibers to the photomultiplier tubes, which are located at the fringes of the magnetic field two meters away.

Next is the straw drift chamber (SDC), operating since 1994 and installed expressly for the measurement of the ρ^0 mass in 3He , with the objective of improving the momentum resolution for the detection of the $\rho^0 \rightarrow \pi^+\pi^-$ decay channel [29]. The SDC consists of two semi-circular cylindrical sections, each containing four layers of vertical cells. The “straw” cells have tube-shaped cathodes which induce a radial electric field, and consequently have a regular field

definition and high position resolution ($\sim 150 \mu\text{m}$). The SDC was designed to preserve the π -sr large acceptance prior to its installation, to not impose extensive modifications of the spectrometer, and to not induce significant energy losses to traversing particles by keeping its thickness to minimum. The installation of the SDC required, nonetheless, the replacement of the IH from an earlier set of scintillators with the one described above.

Surrounding the SDC are two semicircular cylindrical drift chambers (CDC) subtending angles from 15° to 165° on both sides of the beamline in the horizontal plane, and $\pm 18.3^\circ$ in vertical out-of-plane angles. The CDC is composed of twelve concentric layers of drift cells, yielding a $\sim 250\text{-}300 \mu\text{m}$ horizontal and 1.5 cm vertical resolution. Together with the SDC, they are used to determine the planar momentum and emission angle of the charged particles traversing them, and the vertex position of trajectory crossings.

The outer set of 33 scintillator elements comes next, serving as the outer hodoscope (OH), with PMT's attached at both ends to help determine the track angle relative to the median plane. The two sets of hodoscopes, IH and OH, measure the TOF corresponding to the tracked trajectories.

Other components of the TAGX spectrometer include 4 sets of $155 \text{ mm} \times 50 \text{ mm} \times 5 \text{ mm}$ e^+e^- background veto counters positioned along the OH arms in the median plane. The veto counters eliminate charged-particle tracks registering within $\Delta z = \pm 2.5 \text{ mm}$, mostly affecting forward-focused e^+e^- pairs produced copiously downstream from the target, but having a small effect on $\pi^+\pi^-$ events.

C. Data acquisition and calibration

The channel of interest being $\pi^+\pi^-$ production from the decay of the ρ^0 meson, two-charged particle coincidences on opposite sides of the beam axis were required of the trigger. Two levels of triggering are implemented in order to optimize the data acquisition electronics. The pretrigger

$$\mathcal{PT} = IH_L \cdot IH_R \cdot \sum_{i=1}^8 TAG_{i_{back}} \cdot \overline{EM}_{front} \quad (3)$$

is generated within 100 ns from the occurrence of an event. A coincidence of a left and right IH hit with a backing tagger hit is required, and not rejected by the forward e^+e^- veto counters. The main trigger

$$\mathcal{MT} = \mathcal{PT} \cdot OH_L \cdot OH_R \cdot \sum_{i=1}^{32} TAG_{i_{front}} \cdot \overline{Inhibit} \quad (4)$$

requires the coincidence of the pretrigger with a left and right OH hit and a forward tagger hit, not rejected by the computer inhibit signal. A window of 400 ns is available between the \mathcal{PT} and the \mathcal{MT} , after which the CAMAC is cleared for the next \mathcal{PT} . Typical counting rates are 2 kHz and 30 Hz for the \mathcal{PT} and \mathcal{MT} , respectively.

The calibration of the scintillation counters and the CDC and SDC have been the subject of extensive effort [20,29,31]. More recently, a series of modifications implemented in the track fitting algorithms has resulted in significant improvements, mainly in the planar-momentum resolution [32]. It is the tracking that is discussed next.

The CDC consists of four groups of three-wire layers (Fig. 1). The last layer of wires for each group was intended for charge division readout and had not been employed in the past [20]. Instead, hits from the eight remaining CDC layers were used for the reconstruction of the planar momentum p_{xy} , emission angle θ_{sc} , and vertex position (see also Section III B). This earlier eight-layer tracking procedure did not incorporate the SDC information either, thus resulting altogether in a less-than-optimal momentum resolution. Since longer effective lengths of reconstructed tracks result in higher-quality fits, however, TDCs from the last layer of wires of the fourth group has been implemented for the first time in the present analysis. Furthermore, the SDC data have also been used for the first time, a combination which yields an overall improvement in the planar momentum resolution estimated to be $\sigma_{p_{xy}}/p_{xy} = 0.0892p_{xy} + 0.0057$, compared with $\sigma_{p_{xy}}/p_{xy} = 0.1150p_{xy} + 0.0078$ from the 8-layer CDC analysis [32]. For a particle of $p_{xy}=300$ MeV/c, this amounts to a 40% improvement in the planar momentum resolution. The corresponding improvement in the vertex position is reflected in Fig. 2, and has allowed for more stringent tests in the selection of two-track events which originate from the target area. A minor improvement has also been noted in the emission angle resolution, which stays relatively constant at $\sigma_{\varphi} \sim 0.3^{\circ}$ throughout the range of typical planar momenta $100 \text{ MeV}/c \leq p_{xy} \leq 500 \text{ MeV}/c$ [32].

The steps involved in the tracking of trajectories through the SDC and CDC may be summarized in the following: The CDC TDCs operate in “common-stop” mode, with the start determined from each CDC sense wire and the stop from the IH [20]. The CDC drift times are first corrected by the corresponding TDC timing offsets. The drift-length to drift-time relation is determined next, per layer of CDC wires, as a fifth-order polynomial. This is an iterative process, where an initial set of parameters is used to reconstruct a sample of well-defined high-momentum tracks. The reconstructed trajectories yield a new set of parameters, and the procedure is repeated until the convergence condition is reached, namely that the residual root mean square (RRMS) improvement over the final two cycles is no better than 0.5%.

Once a CDC track has been reconstructed, a similar procedure is followed for the SDC, where first the TDC timing offset is determined, and subsequently a SDC length-to-time relationship is extracted. This accomplished, “best” SDC tracks are identified, which qualify as candidate extensions of a selected CDC track. Typically, 2-4 SDC tracks are selected as possible extensions of a reconstructed CDC track when all four SDC layers have registered a hit, to

a maximum of 8 candidate tracks if one SDC layer is missed. The SDC tracks are approximated by straight-line segments, since the error in the position of even the slowest particles which may be expected to result in valid two-track events is within the 150 μm tolerance of the SDC. Finally, the SDC candidates are matched with the CDC reconstructed track, by requiring the minimal CDC + SDC RRMS of the combined track.

The obtained TOF resolution σ_t is better than 380 ps [20]. The TOF is used for particle identification, as well as for the determination of the particles' OH position (along the \hat{z} -axis in the TAGX frame as shown in Fig. 1).

III. DATA ANALYSIS

The data presented in this report were collected in two periods, with ${}^3\text{He}$ and empty-target measurements in each. The superior quality of the photon beam, and a longer running period, resulted in better statistics and a higher ratio of $\pi^+\pi^-$ to accidental triggers for the second phase. This is reflected in the tagger efficiencies and radiator out/in ratios, defined in Eq. (2), which during the later part of the experiment were generally improved. A total of 16,366 $\pi^+\pi^-$ events have been identified from the analysis of two-track events, comprising 73% of the total number of reconstructed events, the remaining being of three (23%) or more tracks (<4%). With the extraction of the $\pi^+\pi^-$ yield Y , the total cross section σ_T is determined from the relation

$$\sigma_T = \frac{Y}{N_T N_\gamma \eta_{\pi^+\pi^-} \eta_{daq}} \quad (5)$$

where N_T (nuclei/cm²) is the ${}^3\text{He}$ target density seen by the photon beam, and N_γ is the incident photon flux. The efficiencies η_{daq} and $\eta_{\pi^+\pi^-}$ account for the data-acquisition livetime and $\pi^+\pi^-$ detection efficiencies. The latter, which is in the range of 2.7-6.8% for the ρ^0 channels, is determined by dedicated MC routines and is reaction-channel specific (see Ref. [20]).

A. Empty target background

In Section II A, the extraction of the tagger efficiencies, and the normalization of the tagger scalers to reflect the number of photons incident on the target, were discussed. These are utilized in determining the appropriate factor by which empty-target spectra are scaled prior to their subtraction from the corresponding ${}^3\text{He}$ -target spectra, for the removal of target background counts. The procedure is briefly summarized in the following steps.

At regular intervals throughout each of the ${}^3\text{He}$ -target and empty-target running periods, the lead-glass Čerenkov counter is employed in dedicated reference runs to determine the quantities η_i and \mathcal{R}_i , as described in Section II A.

The total number of photons incident on the target per experiment is extracted as the sum of the raw scaler counts T_i , recorded for each run, corrected by the efficiency and out/in ratios for that run, according to Eq. (2), and weighted by the normalized energy distribution of the scattered electrons. In particular, η_i and \mathcal{R}_i for each run are calculated from the corresponding quantities of the reference runs, on the assumption that they vary linearly with the raw scaler counts accumulated between runs. The ratios of photon fluxes between each ${}^3\text{He}$ -target and its corresponding empty-target experiment yield the scaling factors by which the latter are normalized prior to subtraction from the former. The x-coordinate spectrum of the two-pion crossing vertex after background subtraction, indicative of the accuracy of this procedure, is shown in Fig. 3.

B. Experimental observables

The calibration procedure, discussed in Section II C, allows the extraction of the planar momentum p_{xy} , the polar emission angle in the median plane φ , the planar trajectory length l_{xy} from the SDC + CDC particle tracking, and the time of flight and z-coordinate (OH position) from the IH and OH scintillators:

$$\begin{aligned} t &= \frac{1}{2} (t_{OH}^{up} + t_{OH}^{down}) - t_{IH} \\ z &= \frac{1}{2} (t_{OH}^{down} - t_{OH}^{up}) v_{eff} \end{aligned} \quad (6)$$

The up-down indices correspond to the timing measurements at the two ends of the OH, and v_{eff} is the effective light transmission velocity in the scintillator material. These yield the primary observables (Figs. 4,5)

$$\begin{aligned} \theta_{dip} &= \tan^{-1} \left(\frac{z}{l_{xy}} \right) \\ p &= p_{xy} / \cos \theta_{dip} \\ l &= l_{xy} / \cos \theta_{dip} \\ \beta &= l / ct \\ m &= p / \beta \gamma c \\ \theta_{sc} &= \cos^{-1} \left(\cos \varphi \frac{p_{xy}}{p} \right) \end{aligned} \quad (7)$$

where θ_{dip} is the out-of-plane dip angle, p and l the total momentum amplitude and three-dimensional trajectory length, and θ_{sc} the scattering angle with respect to the incident beam (Fig. 5). A left-right asymmetry noted in the scattering angle θ_{sc} spectrum (Fig. 5d) has been reproduced in the MC simulations.

A coincidence of two charged particles, one on either side of the photon beam, signifies the occurrence of an event (Section II C). A series of tests and cuts in the data set subsequently eliminate all but the $\pi^+\pi^-$ pairs. In particular, first the time-of-flight versus planar momentum spectra are used for particle identification (PID, Fig. 4). The great majority of events including a proton or e^\pm are thus discarded. Cuts on the tagger TDC spectra reject events induced by spurious photons, not corresponding in timing with the beam pulse. Last, pairs with low-confidence tracks (large RRMS), or whose vertex falls outside the target area (Fig. 2) are eliminated, thus completing a first-level selection based on directly measured observables.

For the two-track events that have cleared the tests above, and have been identified as $\pi^+\pi^-$, additional kinematical observables are calculated. At this stage, the few surviving two-track events involving a proton or e^\pm that had been previously misidentified as $\pi^+\pi^-$ by the PID cuts are eliminated as well. The calculated observables include the dipion invariant mass $m_{\pi^+\pi^-}$, the laboratory production angle of the dipion system Θ_{IM} , the missing mass m_{miss} and momentum p_{miss} , the $\pi^+\pi^-$ laboratory opening angle $\vartheta_{\pi^+\pi^-}$, and the π^+ production angle in the dipion center of mass $\theta_{\pi^+}^*$, employed as variables in the MC fitting procedure (Section IV).

Among these observables, the production angle for either one of the two pions in the dipion center-of-mass frame, for example $\theta_{\pi^+}^*$, is singular as a direct experimental observable which, without the aid of simulations or assumptions, points to the presence of the ρ^0 production channel well below the nominal threshold energy. This is discussed next.

C. The $J = 1$ signature of the ρ^0

Among the dominant production channels participating in $\pi^+\pi^-$ photoproduction in the $E_\gamma \sim 1$ GeV region (Section IV A), the $\rho^0 \rightarrow \pi^+\pi^-$ channel alone results in the two pions being produced at a single reaction vertex with the characteristic $J = 1$ angular correlation from the decay of the ρ^0 . In the dipion center-of-mass frame this translates into a pure $\cos^2\theta_{\pi^+}^*$ distribution, where $\theta_{\pi^+}^*$ is the π^+ production angle with respect to the dipion momentum, the direction defined by the latter in the laboratory frame. On the assumption of a slowly-varying $\pi^+\pi^-$ background interfering with the ρ^0 amplitude, the angular distributions are expected to be symmetric around $\theta_{\pi^+}^* = 90^\circ$ for dipion cm energies near the mass of the ρ^0 meson, where the $\rho^0 \rightarrow \pi^+\pi^-$ amplitude peaks. Away from the ρ^0 mass, the resonant amplitude vanishes, and the background processes dictate the shape of the spectra [33]. Thus, above and below the ρ^0 -meson mass, the angular distribution is expected to regain a quasi-isotropic shape due either to the uncorrelated pions produced at two or more reaction vertices, this being the case for the majority of the participating background processes, or from s-wave correlated pions, possibly produced from the decay of the σ

meson (Section IV A).

This technique, of $\rho^{0,\pm}$ identification via the study of the pion-scattering angle in the dipion cm frame, has been extensively used in many previous analyses (e.g. Ref. [34]). The $\theta_{\pi^+}^*$ distribution spectrum, based on the above, is expected to be well-described as $A + B \cos^2 \theta_{\pi^+}^*$, in the vicinity of the dipion invariant mass matching that of the ρ^0 meson, where the $\rho^0 \rightarrow \pi^+ \pi^-$ amplitude peaks.

The $\pi^+ \pi^-$ events in the range of 400-800 MeV/ c^2 in dipion invariant mass have been divided in four 100 MeV/ c^2 bins, which is the finest binning allowed by the data statistics. An additional cut, determined from the MC simulations of the TAGX ρ^0 detection efficiency and kinematical considerations, eliminates those $\pi^+ \pi^-$ events with too small an opening angle to have been the outcome of back-to-back production at a single reaction vertex (see Section IV B). The latter cut results in a further 9-10% reduction in the total number of $\pi^+ \pi^-$ events in the 400-800 MeV/ c^2 dipion invariant-mass region, affecting only events from background processes, effectively boosting the $\rho^0 \rightarrow \pi^+ \pi^-$ amplitude relative to the background (Fig. 6).

The 500-600, and 600-700 MeV/ c^2 regions (Figs. 6b,c) clearly demonstrate the $J = 1$ fingerprint of the ρ^0 meson decay. The deviation from $\cos^2 \theta_{\pi^+}^*$ toward ± 1 is reproduced in MC simulations of the $\rho^0 \rightarrow \pi^+ \pi^-$ process, and it is shown to be the effect of the TAGX detection efficiency, stemming from the two-track detection requirement (see Section IV B and Fig. 7). The quasi-resonant $\rho^0 \rightarrow \pi^+ \pi^-$ amplitude over the 500-700 MeV/ c^2 dipion invariant-mass range points to a substantially reduced ρ^0 mass *beyond* the trivial apparent lowering, which is the artifact of probing the lower tail of the ρ^0 mass distribution with low-energy photons (Section V B).

IV. SIMULATIONS

The MC simulations constitute an integral part of the data analysis by determining the process-dependent detection efficiencies of the spectrometer, guiding the assignment of the weight to each of the contributing production mechanisms, and, ultimately, leading to the extraction of the medium-modified ρ^0 mass.

The steps involved in the simulations and fitting algorithm can be outlined as follows:

- Eleven individual $\pi^+ \pi^-$ production channels are coded into MC generators (Section IV A). These eleven processes are considered to account for the full $\pi^+ \pi^-$ photoproduction yield in the $\gamma + {}^3\text{He}$ reaction. Twelve distributions of six kinematical observables, with cuts aiming to separate the bound ${}^3\text{He}$ from the dissociated ppn final state, are simulated for each production channel and each of four ΔE_γ energy bins (Section IV B).

The analysis of the MC events is identical to that of the experimental data, and yields the process-dependent spectrometer acceptance (Section IV B).

- The simulated spectra for nine of the above elementary processes (Section IV A), including background and ρ^0 production channels with the nominal $m_{\rho^0}=770$ MeV/ c^2 mass, are combined. The twelve spectra of each process are adjusted with a common strength parameter within each of the four ΔE_γ bins before being added together. Subsequently, all twelve simulated spectra are fitted simultaneously to the corresponding experimental ones, yielding the nine strength parameters independently for each ΔE_γ bin. From the latter, and the spectrometer acceptances, total cross sections are extracted for each of the nine production processes, and compared with independently established ones. Adjustments to the starting values and fitting constraints are made in iterative steps until satisfactory agreement is reached.
- The procedure is repeated for all eleven production channels, including the addition of two more processes (Section IV A) with a modified ρ^0 mass $m_{\rho^0}^*$ in the range 500-725 MeV/ c^2 , but common for both the 3He and breakup ppn final states. The ρ^0 mass corresponding to the best fit for each ΔE_γ bin is quoted in this report as the medium-modified $m_{\rho^0}^*$ mass (Section V A).
- Exploratory fits are attempted, decoupling the 3He and breakup ppn final states with respect to $m_{\rho^0}^*$, as well as modifying the width $\Gamma_{\rho^0}^*$ (Section V B).

The principal aspects of this algorithm are elaborated below.

A. Production channels

Several mechanisms are known to contribute to $\pi^+\pi^-$ photoproduction. Recent experiments for photon energies between 450 - 800 MeV at MAMI, using the large-acceptance spectrometer DAPHNE and high-intensity tagged photon beams, and in the range 1 - 2.03 GeV with the SAPHIR detector at ELSA [35], have provided accurate measurements of the reaction $\gamma p \rightarrow \pi^+\pi^-p$ [36,37,38]. These have motivated several theoretical models, which concur in their interpretation of the data as $\pi^+\pi^-$ photoproduction predominantly through the $\pi\Delta(1232) \rightarrow \pi^+\pi^-N$, and the $N^*(1520) \rightarrow \pi\Delta \rightarrow \pi^+\pi^-N$ channels [39,40,41]. In the nuclear medium, the propagators of baryonic resonances require renormalization, and, in addition, many-body effects caused by pion rescattering (FSI) are known to interfere with the lowest-order reaction mechanism of two-pion photoproduction on the nucleon [42]. These medium

modifications affect both the strength and the peak position of the cross-section spectra for the various interfering channels, relative to the corresponding processes on a free nucleon. Nonetheless, the $\Delta(1232)$ and $N^*(1520)$ resonances remain the leading channels in photon-induced reactions in the nuclear medium, as has recently been verified by total photoabsorption cross-section measurements on nuclei [43]. In the latter, substantial contributions were also attributed to the nucleonic excitations $P_{11}(1440)$ and $S_{11}(1535)$, primarily, which largely overlap with the $N^*(1520)$ resonance in medium-modified mass and width.

The double- Δ is another channel that has been verified in photoabsorption measurements on the deuteron [44,45], a process that has also been modelled theoretically [46]. The photon is absorbed on two nuclei, exciting $\Delta(1232)$ resonances, in the reaction $\gamma NN \rightarrow \Delta\Delta$, which subsequently decay to produce $\pi^+\pi^-$ pairs.

In addition, three-pion $\pi^+\pi^-\pi^0$ production, associated with 3He disintegration, is kinematically feasible in the energy range probed by the present experiment. However, the limited out-of-plane detector acceptance coupled with appropriate missing-mass cuts minimize the contributions of this mechanism. The experimental measurements available are sparse for this process in the energy regime of interest [36,47,48].

Other possible contributions to the background $\pi^+\pi^-$ count, which, however, were not found to improve the quality of the fit and are presently not included in the simulations, may come from non-resonant three-, four-, and five-body phase space, corresponding to the 3He remaining intact, or breaking-up into dp and ppn respectively. These multi-body phase-space processes are governed solely by energy and momentum conservation, each with a constant transition matrix element [49], and, loosely speaking, accomodate in an average sense all the remaining possible production channels which are too weak to be individually identified.

The contributions of the mechanisms discussed so far have been previously considered in MC simulations, in connection with TAGX $\pi^+\pi^-$ photoproduction data [21,23,25]. In Ref. [23] in particular, where $\pi^+\pi^-$ photoproduction via the ρ^0 channel was first considered, the background processes

$$\gamma + {}^3He \rightarrow \left\{ \begin{array}{l} i) \quad \Delta\pi(NN)_{sp} \\ ii) \quad N^*(1520)(NN)_{sp} \rightarrow \Delta(1232)\pi(NN)_{sp} \\ iii) \quad N^*(1520)\pi(NN)_{sp} \\ iv) \quad \Delta\Delta N_{sp} \\ v) \quad ppn\pi^+\pi^-\pi^0 \end{array} \right\} \rightarrow ppn\pi^+\pi^-$$

were included in simulations of non- ρ^0 $\pi^+\pi^-$ contributions, as well as final-state interactions (FSI) following the ρ^0 decay (see process *ix*) below). The index *sp* signifies spectator nucleons. The empirical values from Ref. [43] were used

for the $\Delta(1232)$ mass and width and for the $N^*(1520)$ mass, but the fit improved with the $N^*(1520)$ width doubled relative to Ref. [43]. This *ad hoc* increase effectively incorporates the near-by resonances $P_{11}(1440)$ and $S_{11}(1535)$, which largely overlap with the $N^*(1520)$, but cannot be resolved within the sensitivity of the data. Alternate fits were performed with the $N^*(1520)$ replaced by the Roper $N^*(1440)$ and including five-body phase space. The two methods yield comparable masses for the ρ^0 , but the former is preferred as it results in a better fit.

Additional improvements in the fitting procedure, relative to the analysis of Refs. [21,23,25], include the modification of the MC generators to account for the angular momentum of all $\rho^0 \rightarrow \pi^+\pi^-$ and intermediate Δ -resonance channels. Furthermore, motivated by recent $\pi\pi$ phase-shift analyses which increasingly show evidence of s-wave contributions from the σ meson, the quasifree σ -decay channel

$$vi) \quad \gamma + {}^3He \rightarrow \sigma ppn \rightarrow \pi^+\pi^- {}^3He$$

has been added, with the σ mass and width parameters from Ref. [50].

Last, $\rho^0 \rightarrow \pi^+\pi^-$ photoproduction has been simulated by means of five distinct generators, namely

$$\gamma + {}^3He \rightarrow \left\{ \begin{array}{l} vii) \quad \rho^0 + {}^3He \rightarrow \pi^+\pi^- {}^3He \\ viii) \quad \rho^0 ppn \rightarrow \pi^+\pi^- ppn \\ ix) \quad \rho^0 ppn \rightarrow \pi^+\pi^- ppn + (FSI) \\ x) \quad \rho^0 + {}^3He \rightarrow \pi^+\pi^- {}^3He \\ xi) \quad \rho^0 ppn \rightarrow \pi^+\pi^- ppn \end{array} \right\} \begin{array}{l} m_{\rho^0} = 770 \text{ MeV}/c^2 \\ 500 \text{ MeV}/c^2 \leq m_{\rho^0}^* \leq 725 \text{ MeV}/c^2 \end{array}$$

where to channels *vii*)-*ix*) and *x*) – *xi*) are ascribed ρ^0 decay outside, and inside the nuclear medium, respectively, the latter probing the medium effect on the ρ^0 mass. The breakup channels have the reaction taking place on a single nucleon, subject to its Fermi motion, with the remaining two nucleons as spectators. Final state πN interaction (FSI) with one of the two spectator nucleons is included in channel *ix*).

B. Fitting procedure

In modelling $\pi^+\pi^-$ photoproduction on nuclei, the distributions of five kinematical observables (Section III B) were simultaneously fitted to the data in Refs. [21,23,25]. These are

1. the dipion invariant mass $m_{\pi^+\pi^-}$
2. the laboratory production angle of the dipion system Θ_{IM}
3. the missing mass m_{miss}
4. the missing momentum p_{miss}
5. the $\pi^+ - \pi^-$ laboratory opening angle $\vartheta_{\pi^+\pi^-}$

to which one additional kinematical observable has presently been added (Section III C), namely

6. the π^+ production angle in the dipion rest frame $\cos\theta_{\pi^+}^*$.

Moreover, in Ref. [21] it was determined that dividing the data sample in $\Delta E_\gamma = 80$ MeV bins provided the optimal compromise between the presumed constancy of the reaction matrix elements, implicit in the MC simulations which only depend on the kinematics, and the requirement of sufficient statistics. The ΔE_γ partitioning of the data is necessary in order to account for the varying energy dependence of the $\pi^+\pi^-$ cross sections from each of the individual production mechanisms. The 80 MeV binning in E_γ has been retained, resulting in four sectors of the data sample from 800 to 1120 MeV, to be referred by their respective central E_γ values (840, 920, 1000, and 1080 ± 40 MeV).

The addition of the $\cos\theta_{\pi^+}^*$ distribution, though not noticeably affecting the overall quality of the fit, nonetheless provides an additional physical constraint which aids the MC fitting algorithm to converge to a more realistic solution. In particular, this kinematical observable uniquely captures a characteristic feature of the contributing mechanisms, which may be classified into three types according to their respective dependence on $\cos\theta_{\pi^+}^*$ (Fig. 7):

- The channel of interest, diffractive $\rho^0 \rightarrow \pi^+\pi^-$, is unique in producing two p-wave correlated pions. The spectrometer response to this mechanism is consistent with the $J = 1$ dependence, and the deviation from the anticipated $\cos^2\theta_{\pi^+}^*$ distribution towards $\sim \pm 1$ reflects the acceptance cut, stemming from the kinematical conditions, set-up geometry, and the two-pion detection requirement (compare the solid curve of Fig. 7 with Figs. 6b,c).
- The background hadronic channels $i) - iv)$ of Section IV A produce two uncorrelated pions at two or more reaction vertices. The angular correlations of these pions are averaged out over 4π sr in simulations, resulting

in featureless $\cos\theta_{\pi^+}^*$ spectra. The spectrometer geometry, however, suppresses the pion acceptance away from $\cos\theta_{\pi^+}^*=0$ (see e.g. the dashed curve of Fig. 7 for the single- Δ production channel). This is a consequence of the fact that channels $i) - iv)$ involve the decay of intermediate baryonic resonances, accompanied by energetic nucleons.

- Three-pion production and the quasi-elastic σ process, $v)$ and $vi)$ of Section IV A, are characterized by featureless $\cos\theta_{\pi^+}^*$ acceptances, as no energetic nucleons are emitted (dotted curve of Fig. 7).

The combination of improvements relative to the analysis of Ref. [23], namely, accounting for the angular momentum in the Δ and ρ^0 channels, and imposing additional physical constraints via the new kinematical observable $\cos\theta_{\pi^+}^*$, resulted in a more accurate treatment of the process-dependent spectrometer acceptances.

The data have been subjected to two additional cuts, one of which enhances the ρ^0 relative to the background channels, and the other facilitates the separation of the bound 3He from the breakup ppn final states. The former is a $\pi^+\pi^-$ opening-angle cut determined from MC simulations, namely $70^\circ \leq \vartheta_{\pi^+\pi^-} \leq 180^\circ$, eliminating two-pion events that could not have been produced back-to-back from the ρ^0 decay (Fig. 8a). This cut is most effective at the higher end of photon energies covered by the experiment, where the ρ^0 identification becomes difficult by an increasingly deteriorating ρ^0 -to-background ratio with increasing E_γ . The latter cut (Fig. 8b) separates events with missing mass in the proximity of the target mass $m_{{}^3He} \approx 2.8 \text{ GeV}/c^2$ (i.e. $2700 \text{ MeV}/c^2 < m_{miss} < 2865 \text{ MeV}/c^2$), from those associated with the breakup of the target nucleus to ppn in the final state ($2865 \text{ MeV}/c^2 < m_{miss} < 3050 \text{ MeV}/c^2$). The combination of the two types of cuts is applied to three of the kinematical observables, resulting in six additional spectra, besides the unselected $\pi^+\pi^-$ distributions 1-6 enumerated earlier. These are:

$$\begin{array}{l}
 7. \ m_{\pi^+\pi^-} \\
 8. \ p_{miss} \\
 9. \ \cos\theta_{\pi^+}^*
 \end{array}
 \left. \vphantom{\begin{array}{l} 7. \\ 8. \\ 9. \end{array}} \right\} \rho^0 - \text{enhanced low missing} - \text{mass data}$$

$$\begin{array}{l}
 10. \ m_{\pi^+\pi^-} \\
 11. \ p_{miss} \\
 12. \ \cos\theta_{\pi^+}^*
 \end{array}
 \left. \vphantom{\begin{array}{l} 10. \\ 11. \\ 12. \end{array}} \right\} \rho^0 - \text{enhanced high missing} - \text{mass data}$$

While the contributing ρ^0 photoproduction mechanisms may not be experimentally distinguishable (Section I), the cuts aim at partitioning the data in biased samples favoring processes which are more prone to probing either the

nuclear mean-field effect (i.e. coherent and exclusive quasifree photoproduction via the distributions 7-9), or a possible nucleonic effect (i.e. the breakup quasifree channel via the spectra 10-12). The three kinematical observables which were subjected to the cuts, namely, the dipion invariant mass, missing momentum, and dipion-cm π^+ production-angle, were selected empirically from the kinematical observables 1-6 as more sensitive to the ρ^0 mass, and therefore more susceptible to possible medium effects.

With a range of $m_{\rho^0}^*$ values, traversing the region 500-725 MeV/ c^2 , and each value kept common for the unselected, as well as the 3He and ppn selected data, the twelve simulated spectra were fitted simultaneously to the corresponding experimental ones, by minimizing a standard χ^2 function with the strengths of the eleven individual processes $i) - xi)$ (Section IV A) as the fit parameters. The four $\Delta E_\gamma = 80$ MeV bins were fitted independently. The optimal $m_{\rho^0}^*$ for each bin is that corresponding to the minimum value of the χ^2 function (Section V A).

In summary, the MC fitting procedure satisfies the following requirements:

- The $\Delta E_\gamma = 80$ MeV binning restricts the energy dependence of the participating processes to the narrowest bin possible without loss of sufficient statistics.
- The six kinematical observables utilized in the fitting are complementary, and account for different physical attributes of the data sample. This imposes far more stringent constraints than an analysis based on only the invariant mass distribution, as in the case of the CERES data [6].
- The simultaneous fitting of selected and unselected data aims at isolating a strong signal from data samples most responsive to possible ρ^0 mass modifications, while also incorporating in the fit the bulk of $\pi^+\pi^-$ events produced in processes less sensitive to such effects.

The outcome of this procedure is the medium-modified ρ^0 meson mass.

V. RESULTS

A. Quality of fit and uncertainties

Beyond the statistical and other experimental uncertainties which are folded into the calibration and analysis of the measured $\pi^+\pi^-$ yields, additional sources of uncertainty are generated by the MC simulations and fitting algorithm. i) The MC event generators depend exclusively on kinematical parameters, neglecting other aspects of the interaction. As an example, the channel $\gamma + {}^3He \rightarrow (np)_{sp}\Delta\pi$ is modelled as $\gamma + {}^3He \rightarrow (np)_{sp}\Delta^{++}\pi^-$, normalized by an

isospin scaling factor to account for the remaining hadronic charge states. This introduces an uncertainty in the amplitude of this process, similar to which are also present in other background hadronic channels. ii) Independent total cross-section measurements of the constituent reactions, serving to anchor their relative strengths in the full $\pi^+\pi^-$ production process, are sparse (e.g. the quasi-elastic σ channel). The strength for some of the individual channels was inferred from indirect sources. iii) Additional quasifree channels and independent measurements to fix their strength are required in order to extract precision cross sections for the background hadronic channels from the data, processes which merit attention on their own behalf. This may become possible following the analysis of three charged-particle events from TAGX experiments, currently in progress.

Despite the caveats above, the medium-modified ρ^0 masses extracted from the MC fitting procedure have remained remarkably stable with respect to variations of the strength parameters of the constituent reactions, within each of the four ΔE_γ bins. This is all the more significant considering that the data are fit simultaneously for twelve spectra of six kinematical observables. In conjunction with the direct $J = 1$ fingerprint discussed earlier, the insensitivity of the fit, within physical constraints, adds confidence to the premise that the medium-modified ρ^0 -meson masses extracted from the MC simulations reflect genuine features of the data sample.

Following the procedure discussed in Section IV, several MC fits have been performed with $m_{\rho^0}^*$ taking on values from a mesh in the range 500-725 MeV/c² (Fig. 9). The steepness of the χ^2 -vs- $m_{\rho^0}^*$ curve is indicative of the sensitivity of the data sample to ρ^0 mass modifications, within each of the four ΔE_γ bins. Using this as a qualitative criterion, the fitting of the 840 and 920 MeV samples, and to a lesser extent of the 1000 MeV sample, have converged to a “best” $m_{\rho^0}^*$, whereas the fit for the 1080 MeV bin is essentially insensitive to variations of $m_{\rho^0}^*$ (Fig. 9).

For each of the 840, 920, and 1000 MeV bins individually, the MC fits (dark circles, triangles and squares respectively in Fig. 9) yield the best $m_{\rho^0}^*$ and an estimate of its uncertainty. This is achieved as follows: a) The uncertainty σ_{χ^2} is assumed common within each bin. This is justified by the fact that both the data set and the reaction matrix elements used by the MC algorithm are common within each bin. b) A polynomial expansion of the MC χ^2 about $(m_{\rho^0}^* - m_0)$, with m_0 in the proximity of the apparent minimum, is assumed to describe well the dependence of the former on the latter. Subsequently a new χ'^2 minimization yields the rank and the coefficients of the polynomial. A third order polynomial gives the best result for the two lower-energy bins, and it is also assumed to provide the best description of the parent population for the 1000 MeV data sample. This procedure also leads to conservative estimates for σ_{χ^2} , in particular 0.019, 0.013 and 0.017 for the 840, 920, and 1000 MeV bins, respectively. c) The polynomial coefficients and σ_{χ^2} estimates are used to derive the optimal $m_{\rho^0}^*$ and an estimate of its uncertainty for each bin. These are:

- $m_{\rho^0}^* = 642 \pm 40 \text{ MeV}/c^2$, $800 \text{ MeV} \leq E_\gamma \leq 880 \text{ MeV}$
- $m_{\rho^0}^* = 669 \pm 32 \text{ MeV}/c^2$, $880 \text{ MeV} \leq E_\gamma \leq 960 \text{ MeV}$
- $m_{\rho^0}^* = 682 \pm 56 \text{ MeV}/c^2$, $960 \text{ MeV} \leq E_\gamma \leq 1040 \text{ MeV}$

The improvement in the medium-modified over the unmodified ρ^0 mass fits is evidenced to varied degrees in all the fitted spectra. The order of the improvement is illustrated for the full (unselected) data in the dipion invariant-mass, $\pi^+\pi^-$ laboratory opening-angle, and missing-momentum distributions for the $840 \pm 40 \text{ MeV}$ and $920 \pm 40 \text{ MeV}$ bins, which are most affected by modifications of the ρ^0 mass (Figs. 10,11).

The dipion invariant mass spectra are not the most sensitive to variations of the ρ^0 mass, among the twelve distributions of six kinematical observables that were employed in the fit. This is seen, for example, in comparing the improvement between the unmodified- and modified-mass dipion invariant-mass with the opening-angle and missing-momentum spectra (Figs. 10,11), where the latter two observables are seen to display a greater sensitivity. This underlines the advantage of a fitting procedure that utilizes multiple complementary kinematical observables as opposed to only the invariant mass, thus capturing additional attributes of the physical process, and resulting in a more realistic analysis.

B. Discussion

The $J=1$ angular momentum signal, discussed in Section III C (Fig 6), as well as the dipion invariant mass spectra from the fit (e.g. Figs. 10a,d for $E_\gamma=840 \text{ MeV}$), would appear to indicate medium-modified ρ^0 masses which are actually *lower* than the values quoted earlier (e.g. compare $m_{\rho^0}^*=642 \pm 40 \text{ MeV}/c^2$ for the 840 MeV bin with the centroid suggested by the dashed curve of Fig. 10a). This apparent discrepancy is misleading, and has its origin in a trivial effective mass lowering driven by phase-space, most pronounced at lower photon energies. This is due to the fact that, at low photon energies, only the lower wing of the ρ^0 mass distribution is kinematically accessible (e.g. Fig. 12 for $E_\gamma=840 \text{ MeV}$ and the $\rho^0 ppn$ final state). The shape and the centroid of the mass distribution for the resulting ρ^0 mesons is primarily dictated by the kinematics, and to a lesser extent by the spectrometer acceptance for the particular ρ^0 -producing process. This effect is implicit in the MC generated ρ^0 spectra, and it is by no means sufficient to account for a mass lowering of the order explicitly observed in the experiment. This is manifest, for example, in comparing the lower solid curves of Figs. 10a,d - for which ρ^0 production is dominated by the ppn final state - with the $J=1$ fingerprint of the ρ^0 in Fig. 6. The loci of the former curves, consistent with the mass distribution

indicated by the histogram of Fig. 12a for $E_\gamma=840$ MeV and the nominal ρ^0 mass, are far too high to be compatible with Fig. 6, with a ρ^0 signal peaking in the range of 500-600 MeV/ c^2 . In contrast, the histogram of Fig. 12b for a lowered ρ^0 mass, and the dashed curve in Fig 10a, are consistent.

Alternate fits were also attempted, to possibly discern additional features from the 840 and 920 MeV bin samples. Decoupling the exclusive 3He from the breakup ppn final states with respect to $m_{\rho^0}^*$ yielded identical masses for the 920 MeV bin, and a somewhat smaller mass for the latter relative to the former channel for the 840 MeV bin. The resulting improvement in the quality of fit, however, is within the uncertainty estimate of σ_{χ^2} . Fits were also performed with $\Gamma_{\rho^0}^*$ fixed to the predicted width at half nuclear density extracted for 3He from Ref. [13], about double the free width Γ_{ρ^0} . A sizeable improvement in χ^2 was noted with the modified width for any mass, compared with the free mass and width case. In all cases, however, the χ^2 is 5-10% larger with $\Gamma_{\rho^0}^*$ than with Γ_{ρ^0} . Moreover, the preferred $m_{\rho^0}^*$ is no higher with the modified than with the free width. In summary, these exploratory fits verify the preference in a reduced ρ^0 mass, but are inconclusive, within the sensitivity of the data, as to whether a width modification is *in addition* supported.

The absence of a conclusive ρ^0 mass-modification dependence from the 1000 and 1080 MeV bins, in contrast to the strong signal from the 840 and 920 MeV bins, is telling as well. Whereas the former are more prone to probing the exclusive channel, and therefore the nuclear mean-field medium effect, the latter are deeper into the subthreshold region, dominated by the breakup channel, and probe distances shorter than the nucleonic radius. To illustrate the range of the ρ^0 processes in different energy regions, we consider the mean decay length l_0 of the ρ^0

$$\begin{aligned} l_0 &= \beta t_0 = \frac{p\hbar}{m_{\rho^0}\Gamma_{\rho^0}c} \\ \beta &= \frac{p}{m_{\rho^0}\gamma c} \\ t_0 &= \gamma\tau_0 = \gamma\frac{\hbar}{\Gamma_{\rho^0}}, \end{aligned} \tag{8}$$

with the nominal mass m_{ρ^0} and width Γ_{ρ^0} for the ρ^0 meson, in the rest frame of either the interacting nucleon, or the 3He nucleus, for the breakup or bound final state (Fig. 13). At low photon energies (e.g. $E_\gamma=840$ MeV, Fig. 13a) the ppn channel dominates ρ^0 photoproduction. This is verified by the fact that the low missing-mass selected data represent less than 10% of the total unselected events, whereas the high missing-mass selected data contribute the great majority of the ρ^0 events and their corresponding distributions are generally consistent with the full (unselected) data. With the ρ^0 mesons produced on the nucleon, and a mean decay length of under 0.5 fm for a substantial portion of them, there is a large overlap of the volume traversed before their decay and the nucleonic volume. To the extent that

the medium modifications of the vector-meson properties depend on the density of the surrounding nuclear matter, it is conceivable that the induced medium effect be dominated by the large densities encountered in the interior of the nucleon, and consequently be far more pronounced than a medium effect induced by nuclear fringe densities. At higher photon energies (e.g. $E_\gamma=1$ GeV, Fig. 13b), both the ppn and 3He final states contribute and the mean decay length increases. Whereas nucleonic densities become increasingly inaccessible, a large overlap of the volume traversed by the ρ^0 before its decay with the 3He nucleus may still induce a weaker nuclear medium effect. Moreover, the possibility of a medium-induced increase in the width Γ_{ρ^0} is in favor of shorter decay lengths (Eq. 8), and therefore further increases the likelihood of accessing regions of large densities either in the nucleon, or the nuclear core. The present results may therefore be suggestive of a moderate medium effect in the realm of the nuclear mean field at near-threshold photon energies, probing normal nuclear densities, turning to a drastic reduction of the ρ^0 mass in the deep subthreshold region, where the ρ^0 decay may be induced in the proximity of the nucleon. These implications, however, need to be further investigated and verified by higher precision and large solid angle experiments [28].

VI. CONCLUSIONS

In summary, the kinematics and final state of the ${}^3He(\gamma,\pi^+\pi^-)X$ reaction have been studied with the TAGX spectrometer and a tagged photon beam in the subthreshold ρ^0 photoproduction region. The bound 3He and breakup ppn components of the ρ^0 channel have been investigated, aiming at the distinction between a nuclear and a possible nucleonic medium effect on the ρ^0 mass. The ρ^0 channel has been aided by the inherent selectivity of the TAGX spectrometer to coplanar $\pi^+\pi^-$ events, and by the choice of 3He as a target with minimal FSI effects without suppression of the ρ^0 amplitude. In any case, the size of target has little effect in the subthreshold region. The $J = 1$ fingerprint of the ρ^0 has been observed in the dipion invariant mass region 500-700 MeV/ c^2 , pointing to a substantial reduction beyond a trivial phase-space governed apparent lowering. This has been verified by MC simulations, incorporating the exclusive and breakup ρ^0 channels, the latter both with and without FSI, as well as background hadronic channels and s-wave correlations. The extracted ρ^0 medium-modified masses, 642 ± 40 MeV/ c^2 , 669 ± 32 MeV/ c^2 , and 682 ± 56 MeV/ c^2 for the 840, 920, and 1000 MeV data bins, suggest a strong medium effect in the deep subthreshold region, requiring large densities that are incompatible with a nucleus as light as 3He , but that are more consistent with the probing of the nucleonic volume. The pattern of decreasing sensitivity with increasing photon energy, with the 1080 MeV bin showing no evidence of a ρ^0 mass-modification signal, hints a moderate mean-field nuclear effect at near-threshold energies. The simulations are inconclusive regarding a medium-modified ρ^0 width.

Further analysis currently in progress for photoproduction on heavier targets (${}^4\text{He}, {}^{12}\text{C}$) and for background contributions (e.g. the $\Delta\pi$ channel) from TAGX experiments, as well as future experiments planned for TJNAF [28], may more accurately isolate the $\rho^0 \rightarrow \pi^+\pi^-$ channel from the background processes, and shed light on the nature of the medium modifications on light vector-meson properties at the interface of hadronic and quark matter.

The authors wish to thank H. Okuno and the staff of INS-ES for their considerable help with the experiment. Furthermore, the authors acknowledge the very insightful discussions with P. Guichon, M. Ericson, A. Thomas, and A. Williams during the Workshop on Hadrons in Dense Matter (Adelaide, March 10-28, 1997), as well as the discussions with N. Isgur at Jefferson Lab. This work has been partially supported by grants from INS-ES, INFN/Lecce, NSERC, and UFF/GWU.

* Present address: GSI, KPI/Leptonen, Planckstrasse 1, 64291 Darmstadt, Germany

E-mail: kagarlis@gsi.de

† Present address: Department of Physics, University of Evansville, Evansville, Indiana 47722

‡ Present name: KEK-Tanashi Division

- [1] A. Casher, Phys. Lett. B **83**, 395 (1979).
- [2] R. Pisarsky, Phys. Lett B **110**, 155 (1982).
- [3] T. Hatsuda and S. H. Lee, Phys. Rev. C **46**, R34 (1992).
- [4] G. E. Brown, Nucl. Phys. A**488**, 689 (1988)
- [5] G. E. Brown and C. M. Rho, Phys. Rev. Lett. **66**, 2720 (1991).
- [6] CERES Collaboration, G. Agakichiev *et al.*, Phys. Rev. Lett. **75**, 1272 (1995);
G. Agakichiev *et al.*, Phys. Lett. B, in print.
- [7] HELIOS-3 Collaboration, M. Masera *et al.*, Nucl. Phys. **A590**, 93c (1995);
NA50 Collaboration, E. Scomparin *et al.*, *ibid.* **A610**, 331c (1996).
- [8] G. Q. Li, C. M. Ko and G. E. Brown, Phys. Rev. Lett. **75**, 4007 (1995).

- [9] W. Cassing, W. Ehehalt and C. M. Ko, Phys. Lett. **B363**, 35 (1995);
C. P. de los Heros, Ph.D. Dissertation, Weizmann Institute, 1996.
- [10] R. Rapp, G. Chanfray and J. Wambach, Nucl. Phys. **A617**, 472 (1997).
- [11] W. Cassing, E. L. Bradkovskaya, R. Rapp, and J. Wambach, Phys. Rev. C **57**, 916 (1998).
- [12] B. Friman and H. J. Pirner, Nucl. Phys. **A617**, 496 (1997).
- [13] F. Klingl, N. Kaiser, and W. Weise, Nucl. Phys. **A624**, 527 (1997).
- [14] G. E. Brown, G. Q. Li, R. Rapp, M. Rho, and J. Wambach, nucl-th/9806026, to be published in Acta Phys. Polon.
- [15] NA50 Collaboration, M. Gonin *et al.*, Nucl. Phys. **A610**, 404c (1996).
- [16] G. E. Brown *et al.*, Phys. Rev. Lett. **60**, 2723 (1998), and references therein.
- [17] E. J. Stephenson *et al.*, Phys. Rev. Lett. **78**, 1636 (1997).
- [18] R. Koniuk and N. Isgur, Phys. Rev. D **21**, 1868 (1980).
- [19] K. Saito, K. Tsushima and A. W. Thomas, Phys. Rev. C **56**, 566 (1997).
- [20] K. Maruyama *et al.*, Nucl. Instr. Meth. **A376**, 335 (1996).
- [21] D. G. Watts *et al.*, Phys. Rev. C **55**, 1832 (1997).
- [22] H. Alvensleben *et al.*, Nucl. Phys. **B18**, 333 (1970).
- [23] G. J. Lolos *et al.*, Phys. Rev. Lett. **80**, 241 (1998).
- [24] Z. Papandreou *et al.*, submitted to Phys. Rev. C.
- [25] G. M. Huber, G. J. Lolos and Z. Papandreou, Phys. Rev. Lett. **80**, 5285 (1998).
- [26] G. E. Brown, M. Buballa and M. Rho, Nucl. Phys. **A609**, 519 (1996).
- [27] P. A. M. Guichon and M. Ericson, private communication.
- [28] G.J. Lolos *et al.*, “Medium Modifications of Vector Mesons in the Subthreshold Region”, JLab Proposal (submitted to PAC-15).
- [29] G. Garino *et al.*, Nucl. Instr. Meth. **A388**, 100 (1997).

- [30] M. Harada *et al.*, Nucl. Instrum. Methods Phys. Res. A **276**, 451 (1989);
S. Kato *et al.*, *ibid.* **290**, 315 (1990);
S. Kato *et al.*, *ibid.* **307**, 213 (1991).
- [31] M. Iurescu, M.Sc. Thesis, University of Regina, 1997, unpublished;
A. Weirnerman, M.Sc. Thesis, University of Regina, 1996, unpublished.
- [32] A. Shinozaki, University of Regina TAGX Collaboration Report, 1998, unpublished.
- [33] I. S. Hughes, *Elementary Particles* (Cambridge University Press, Cambridge, 1985), 2nd ed., pp. 201-202.
- [34] W. D. Walker, J. Carroll, A. Garfinkel, and B. Y. Oh, Phys. Rev. Lett. **18**, 630 (1967).
- [35] W. Scwille *et al.* (SAPHIR Collaboration), Nucl. Instr. Meth. **A344**, 470 (1994).
- [36] F. J. Klein, Ph.D. Dissertation, Bonn IR-96-08 (1996).
- [37] A. Braghieri *et al.*, Phys. Lett. B **363**, 46 (1995).
- [38] F. Härter *et al.*, Phys. Lett. B **401**, 229 (1997).
- [39] J. A. Gomez-Tejedor and E. Oset, Nucl. Phys. **A571**, 667 (1994);
ibid. **A600**, 413 (1997).
- [40] L. Y. Murphy and J. M. Laget, DAPNIA/SPhN 95-42 (1995).
- [41] K. Ochi, M. Hirata, and T. Takaki, Phys. Rev. C **56**, 1472 (1997).
- [42] S. S. Kamalov and E. Oset, Nucl. Phys. **A625**, 873 (1997).
- [43] N. Bianchi *et al.*, Phys. Rev. C **54**, 1688 (1996).
- [44] M. Asai *et al.*, Z. Phys. A **344**, 335 (1993).
- [45] Y. Wada, for the SAPHIR Collaboration, Particles and Nuclei International Conference, Williamsburg, Virginia, 1996
(unpublished).
- [46] J. A. Gomez-Tejedor, E. Oset, and H. Toki, Phys. Lett. B **346**, 240 (1995).
- [47] J. Hannappel, Ph.D. Dissertation, Bonn IR-96-04 (1996).
- [48] The ABBHHM Collaboration, Phys. Rev. **175**, 1669 (1968).

- [49] D. Luke and P. Soding, in “Symposium on Meson-, Photo-, and Electroproduction at Low and Intermediate Energies,” Vol. 59 of *Springer Tracts in Modern Physics*, edited by G. Höhler (Springer-Verlag, Berlin, 1971), p. 39.
- [50] R. M. Barnett *et al.*, *Phys. Rev. D* **54**, 1 (1996).

FIGURES

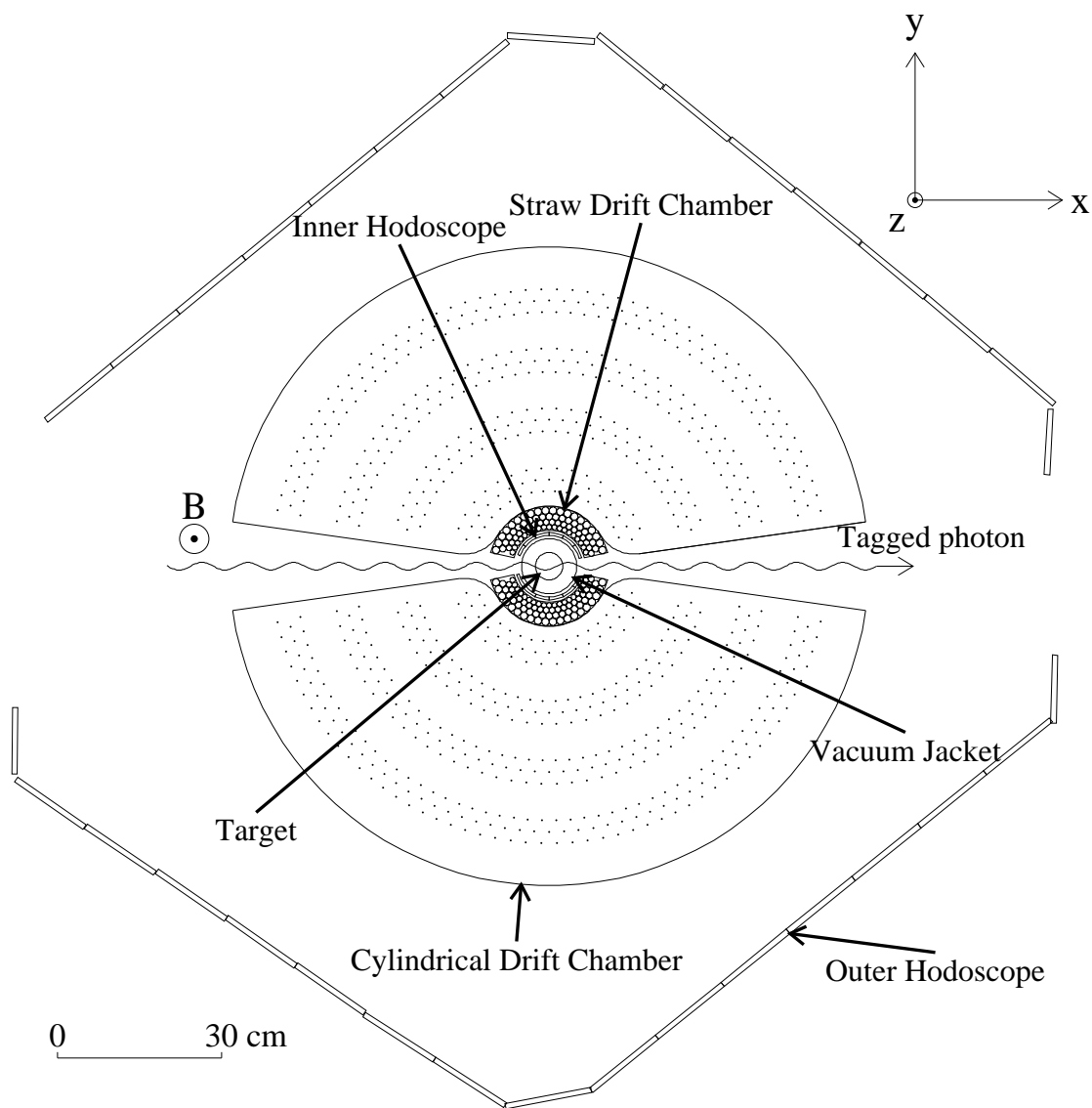


FIG. 1. Components of the TAGX spectrometer: Radially outwards from the target vessel at the center are seen the IH, SDC, CDC, and OH. The TAGX coordinate frame has the \hat{x} -axis pointing in the direction of the photon beam, and the \hat{z} -axis pointing outward from the page in the direction of the 0.5 T magnetic field of the dipole analyzer magnet. Veto counters (not shown in the figure) are positioned along the OH arms in the xy -plane, for e^+e^- -pair rejection, mainly at forward angles.

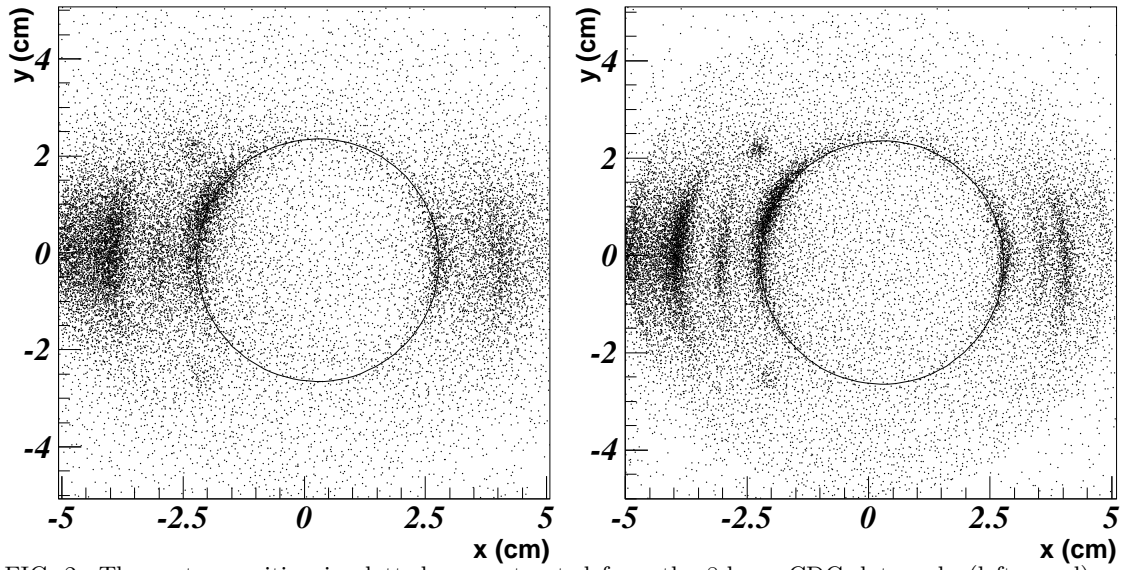


FIG. 2. The vertex position is plotted, reconstructed from the 8-layer CDC data only (left panel), and from the 9-layer CDC and SDC data (right panel), for a set of empty-target runs [32]. The evident improvement in the resolution is discussed in the text. The components of the target vessel, visible in the figure, have been discussed elsewhere [29,30]. The inner ring corresponds to the Mylar wall containing the liquid ${}^3\text{He}$ target, a cylinder 50 mm in diameter. A circle indicating the position of the target container has been drawn, centered at $(x,y)=(2.8\text{ mm},-1.5\text{ mm})$ in the TAGX coordinate frame.

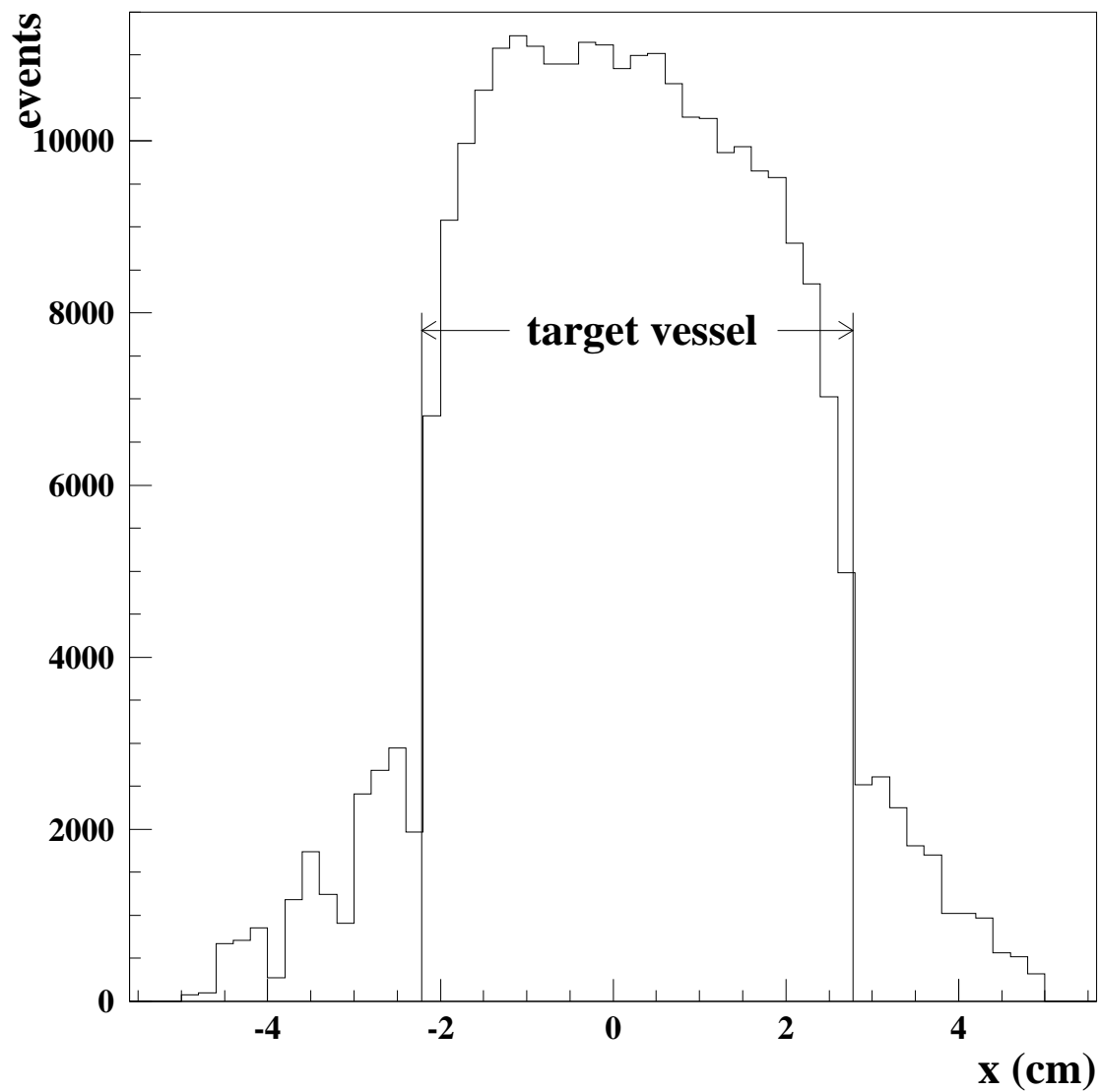


FIG. 3. The x -coordinate of the vertex position after background subtraction is shown, along with the target-vessel walls indicated as lines. Only $\pi^+\pi^-$ events from this target region are considered in the analysis.

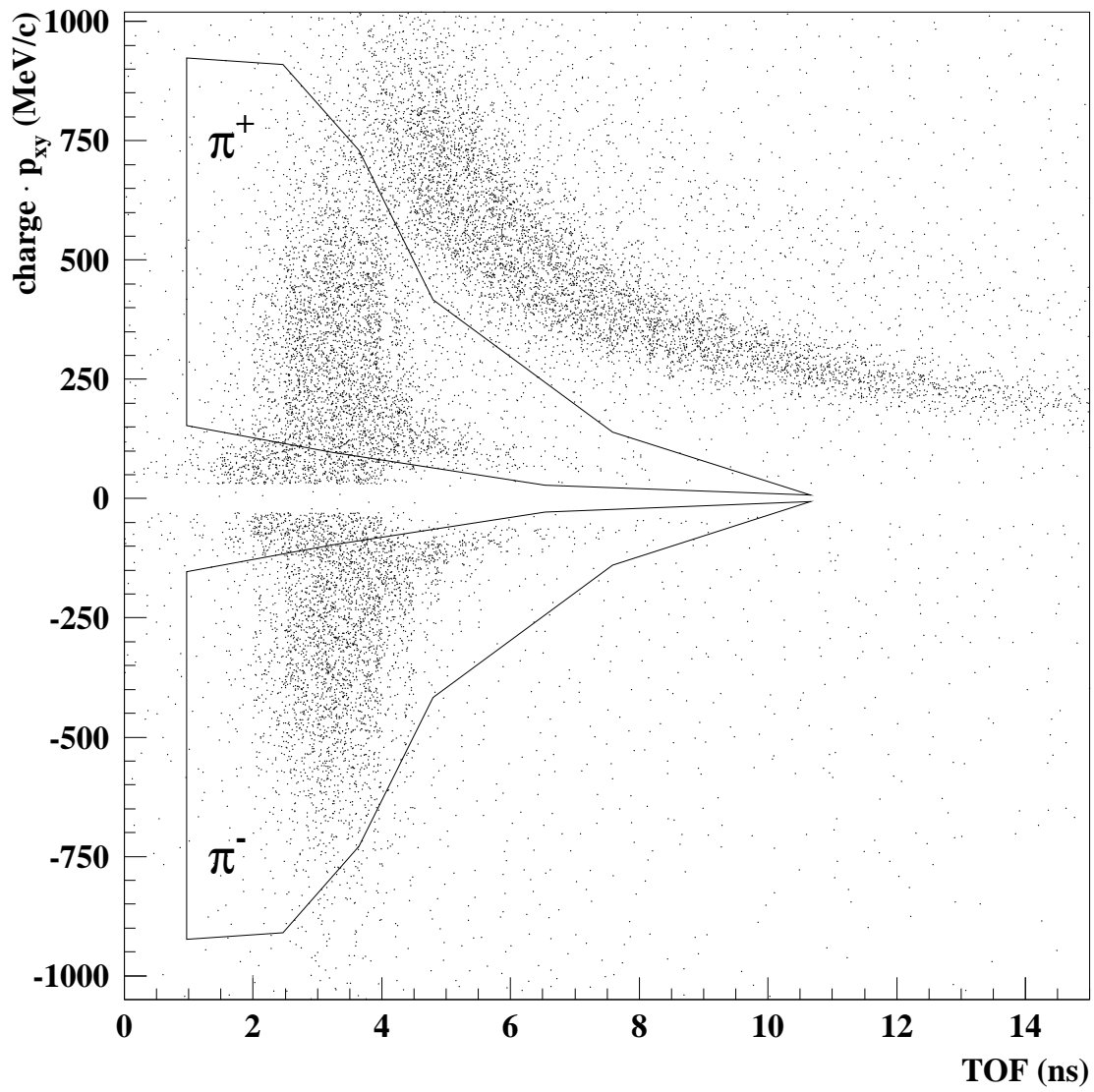


FIG. 4. The TOF-vs-planar momentum spectra, displaying proton (upper-most), π^\pm (in the box cuts), and e^\pm (adjacent to the $p_{xy} = 0$ axis) bands, are used for particle identification.

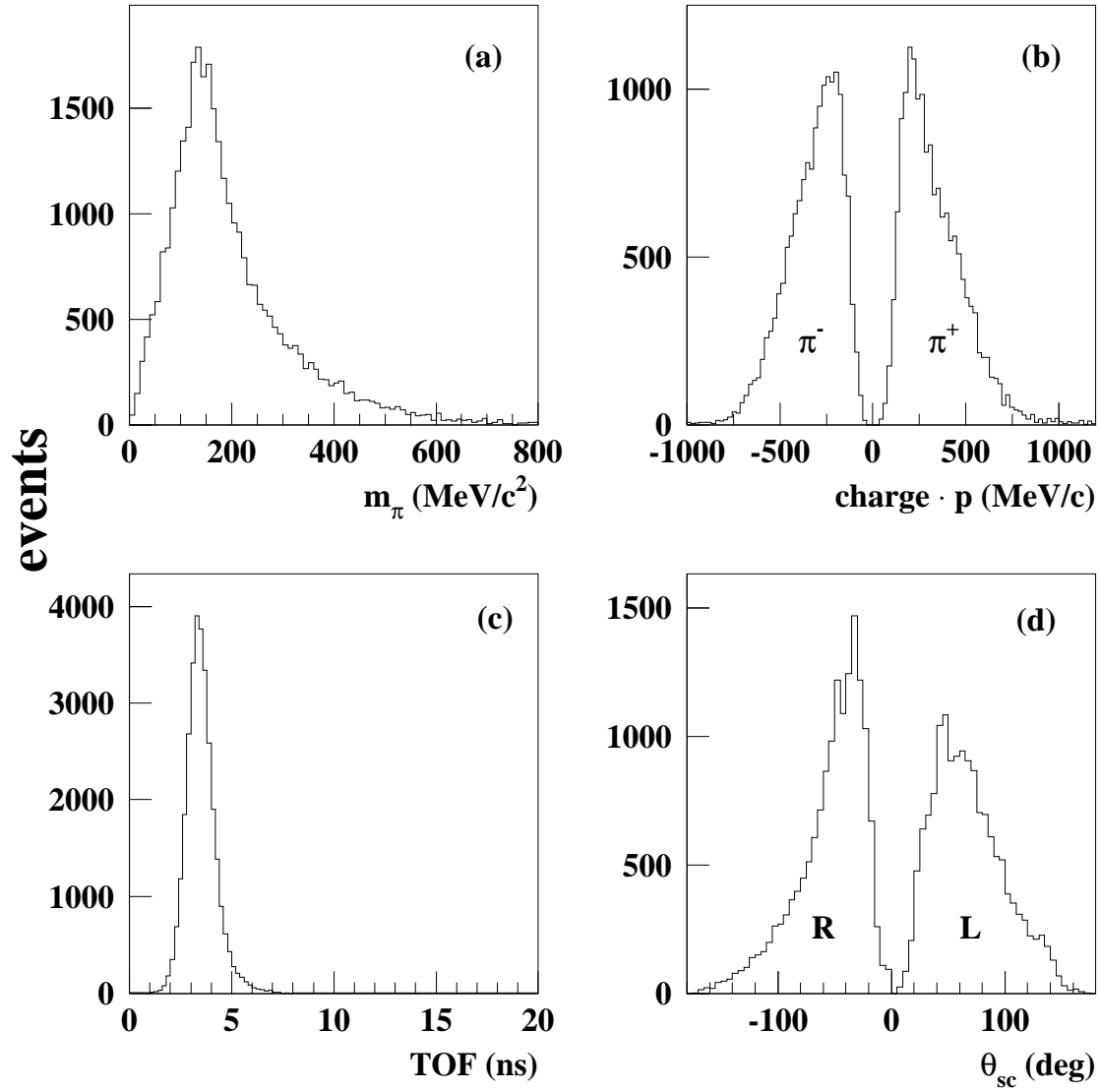


FIG. 5. Some of the kinematical observables for $\pi^+\pi^-$ events, described in the text, are shown. The sign of the momentum corresponds to the pionic charge. The sign of the scattering angle θ_{sc} depends on whether the track registered to the left (>0) or right (<0) of the beam (see Fig. 1).

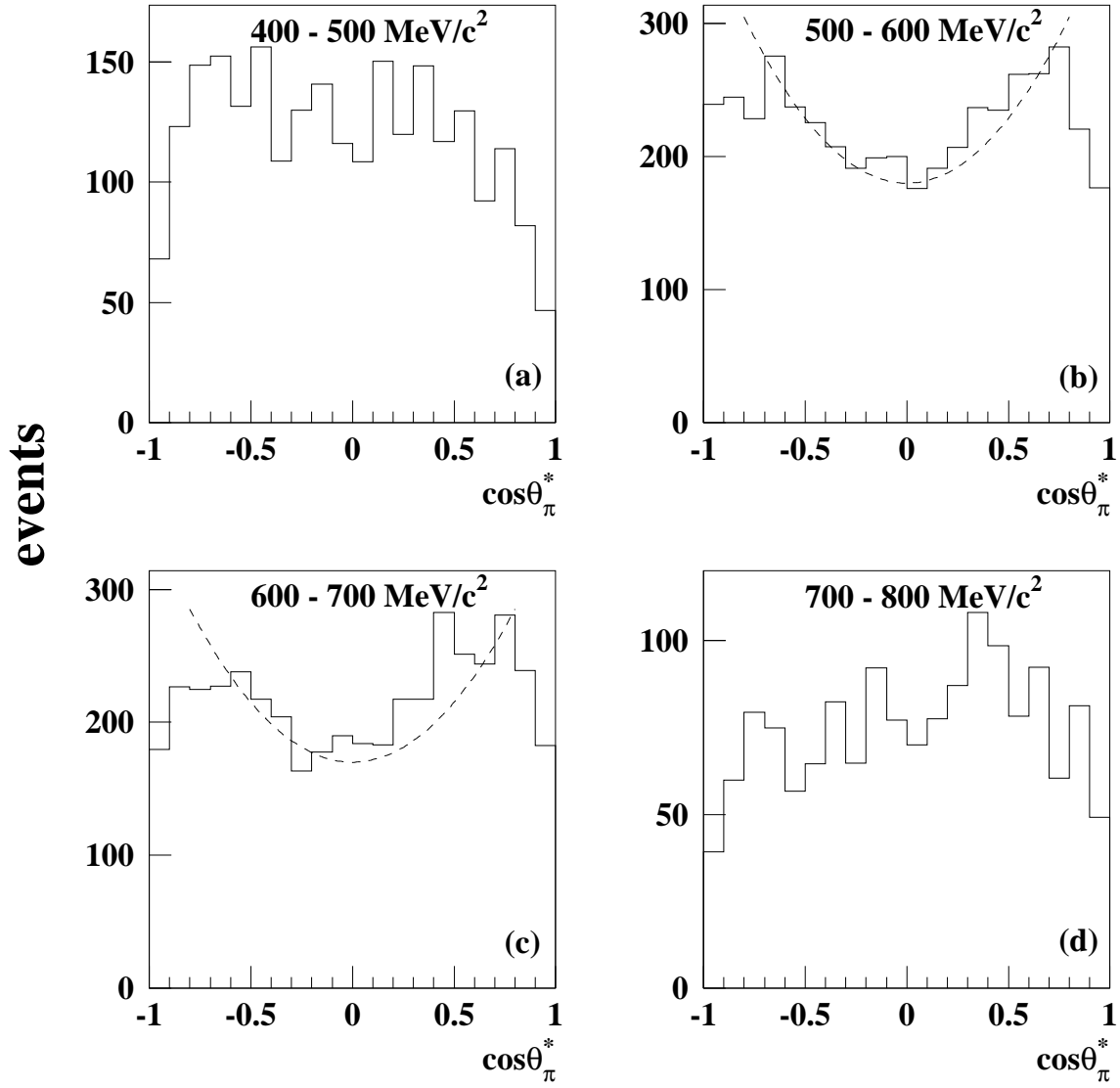


FIG. 6. The $\cos\theta_{\pi^*}$ distribution captures the $J = 1$ signature of the $\rho^0 \rightarrow \pi^+\pi^-$ decay. Panels b) and c) display the $A+B\cos^2\theta_{\pi^*}$ dependence (dashed curve), expected on the basis of the $J = 1$ angular momentum, and the deviation towards ± 1 is due to the spectrometer acceptance.

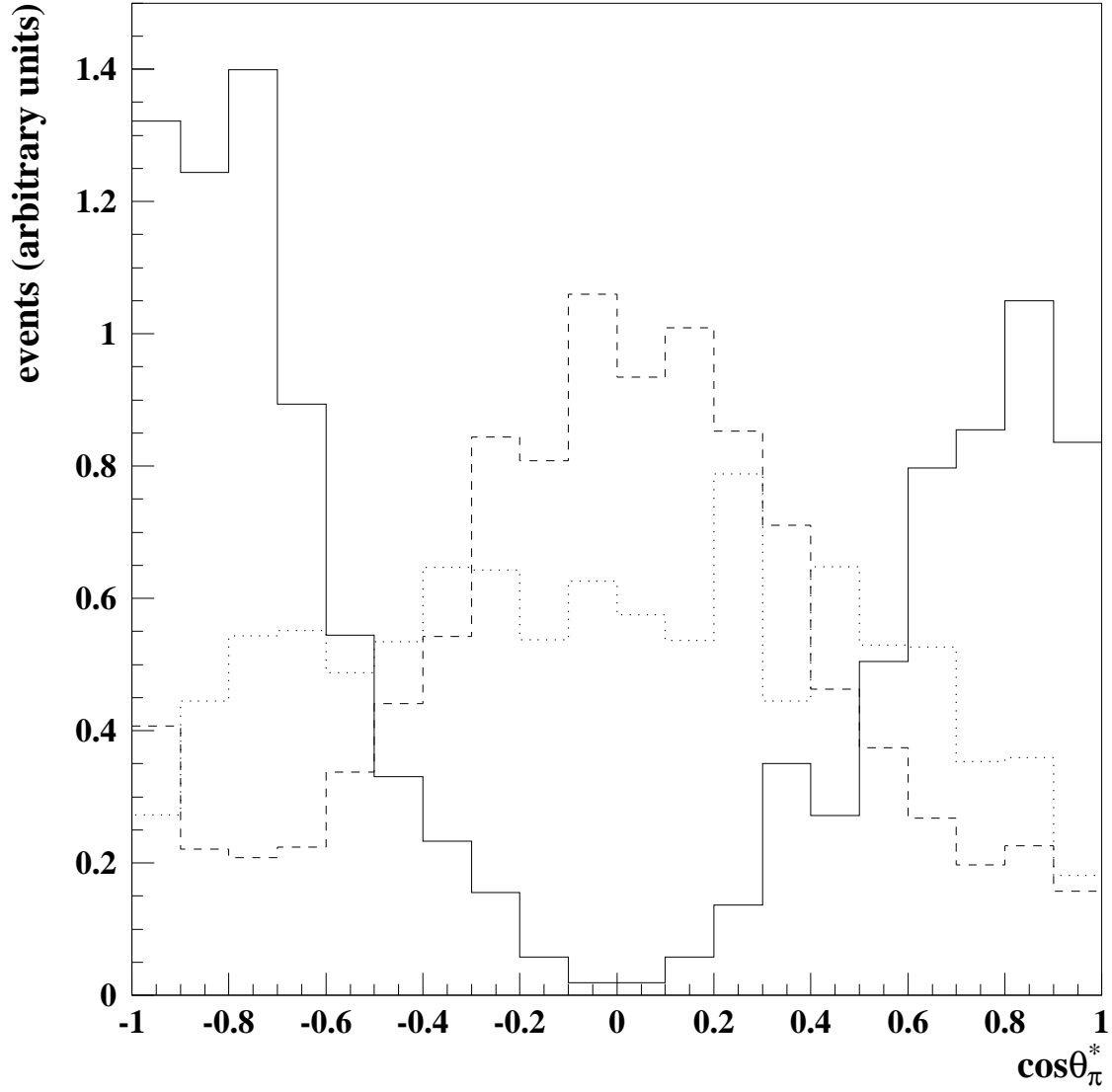


FIG. 7. Simulated events from different processes, taking into account the spectrometer acceptance, have one of three characteristic $\cos\theta_{\pi^+}^*$ profiles. The simulations shown are differential cross sections normalized to unity at $E_\gamma=920$ MeV, and they display the $\cos\theta_{\pi^+}^*$ dependence for three representative reactions: a) $\gamma + {}^3\text{He} \rightarrow \rho^0 ppn \rightarrow \pi^+ \pi^- ppn$ with the nominal m_{ρ^0} (solid curve), b) $\gamma + {}^3\text{He} \rightarrow \pi^- \Delta^{++} pn \rightarrow \pi^+ \pi^- ppn$ (dashes) and c) $\gamma + {}^3\text{He} \rightarrow \sigma ppn \rightarrow \pi^+ \pi^- ppn$ (dots).

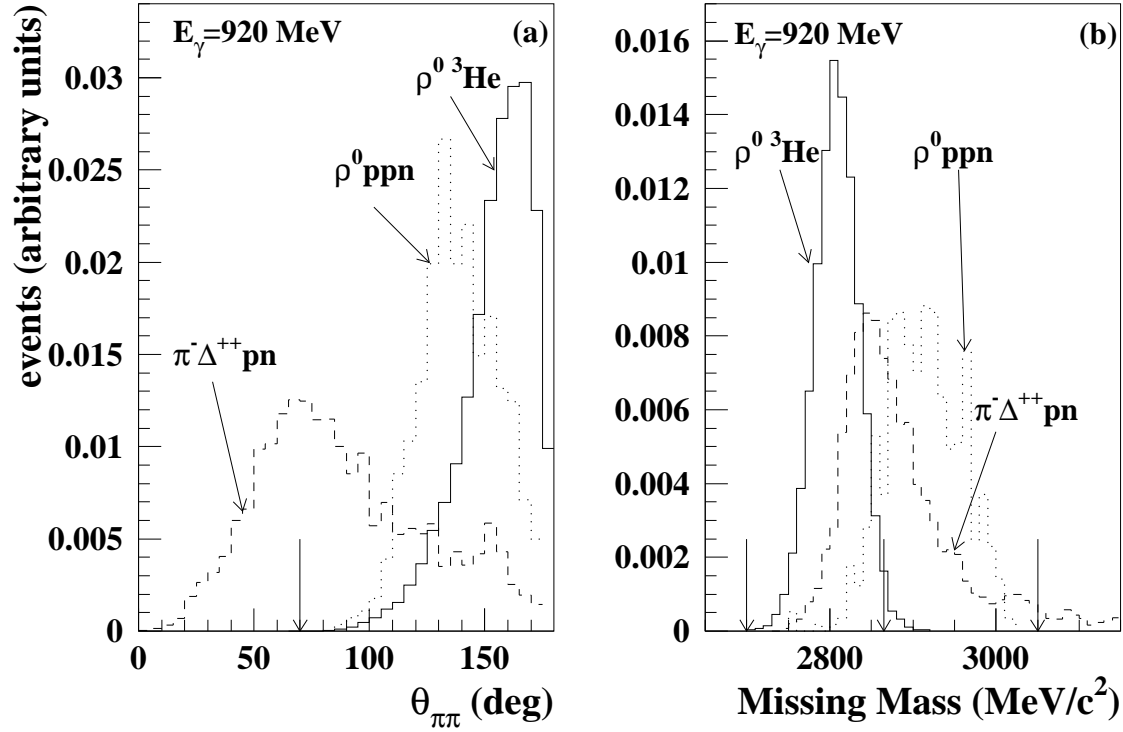


FIG. 8. The effects of the a) $\pi^+ - \pi^-$ opening-angle and b) missing-mass cuts, indicated as arrows in the figure, are shown for the respective simulated spectra of the $\rho^0 {}^3\text{He}$, $\rho^0 \text{ppn}$ and $\pi^- \Delta^{++} \text{pn}$ channels (solid, dotted and dashed lines respectively). The calculations are for $E_\gamma = 920$ MeV and the integral of each distribution is normalized to unity.

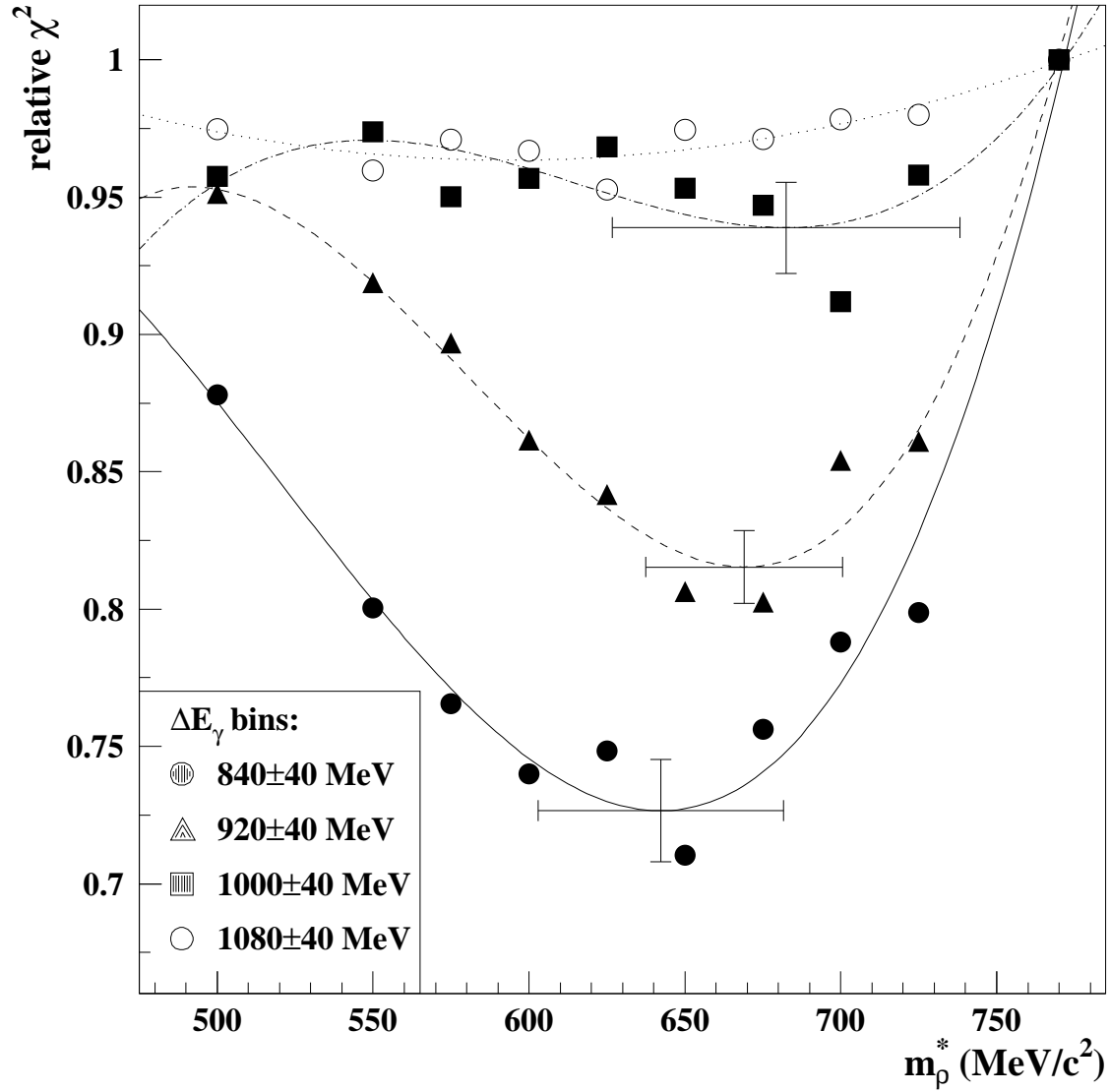


FIG. 9. The dependence of the χ^2 function of the MC fits on the variation of the ρ^0 mass is shown for the four $\Delta E_\gamma=80$ MeV bins. The MC calculations are indicated as points, and fits to third-order polynomials as curves. The fitting procedure yields the best $m_{\rho^0}^*$ per ΔE_γ bin, and estimates of the respective uncertainties.

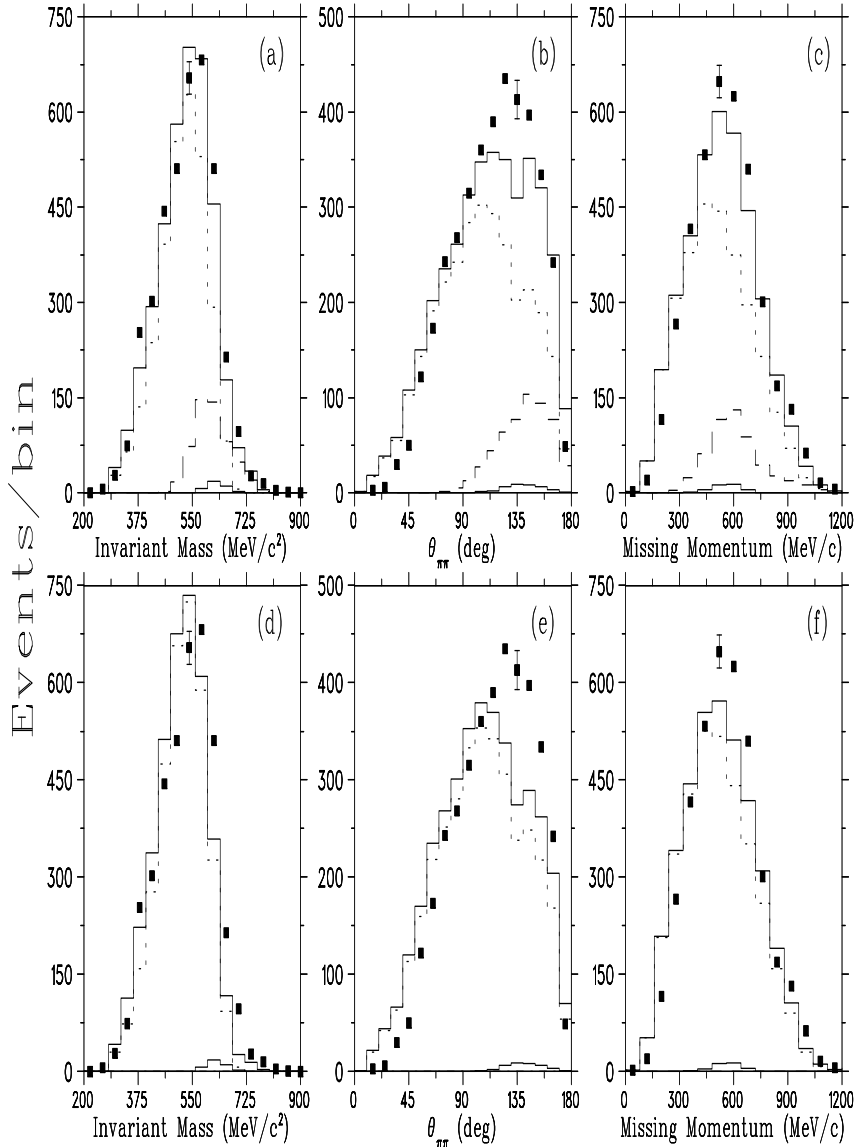


FIG. 10. The dipion invariant-mass (panels a, d), $\pi^+\pi^-$ laboratory opening-angle (panels b, e), and missing-momentum (panels c, f) spectra are shown for the full (unselected) data at $E_\gamma=840 \text{ MeV}$. The solid squares are the data, showing only one representative error bar for clarity. The remaining error bars are comparable and have been included in the fitting. The MC fits shown are: full reaction (upper solid lines), non- ρ^0 background processes (dotted lines), ρ^0 contributions with unshifted mass (lower solid lines), and ρ^0 contributions with $m_{\rho^0}^*=650 \text{ MeV}/c^2$ (dashed lines). The latter are included only in the calculations represented by the top panels (a, b, c). The improvement from bottom to top reflects the effect of including the ρ^0 medium modifications. This improvement is more pronounced for the ρ^0 selected data set, not shown.

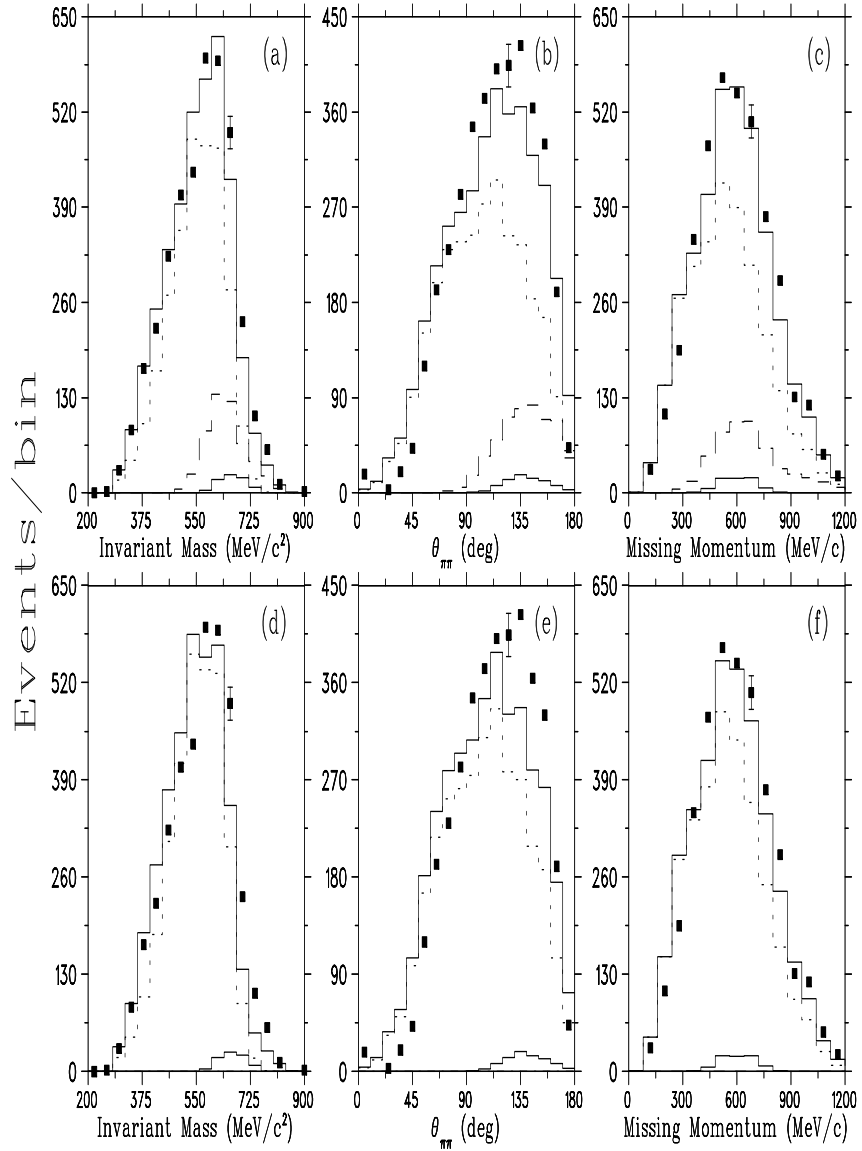


FIG. 11. The data and curves shown are as in Fig. 10, but for the $E_\gamma=920$ MeV bin, and $m_{\rho^0}^*=675$ MeV/ c^2 . It is stressed that the fitting was done independently for each of the four $\Delta E_\gamma=80$ MeV/ c^2 bins, as discussed in the text.

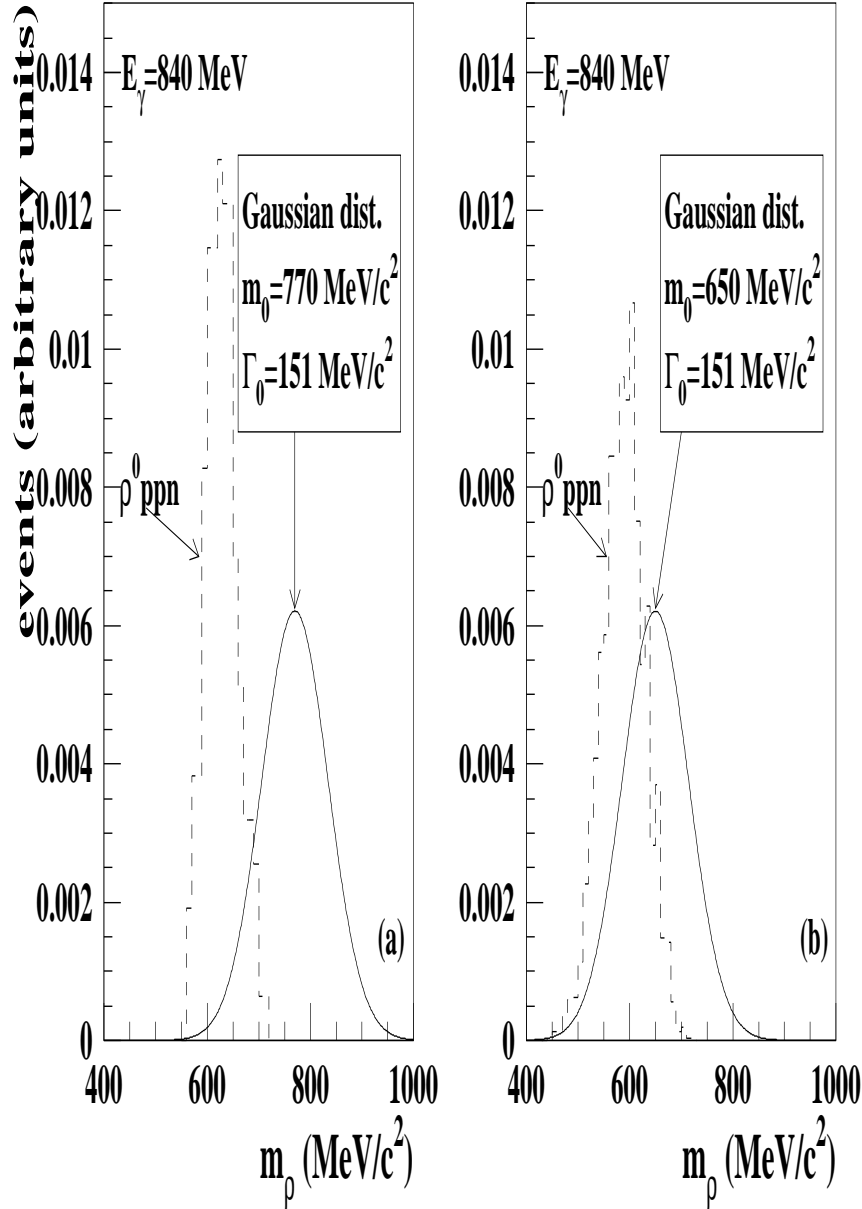


FIG. 12. The trivial ρ^0 mass shift due to kinematic phasespace limitations is illustrated for the quasifree $\gamma + {}^3\text{He} \rightarrow \rho^0 ppn \rightarrow \pi^+ \pi^- ppn$ process at $E_\gamma=840$ MeV, a) for the nominal and b) for a lowered ρ^0 mass. The MC generator randomly selects ρ^0 masses from the Gaussian distributions (solid curves). The histograms (dashed curves) are the resulting m_{ρ^0} spectra whose integrals are normalized to unity, after verification that the reaction is kinematically feasible with the selected mass and that the photoproduced pions are accepted by the spectrometer.

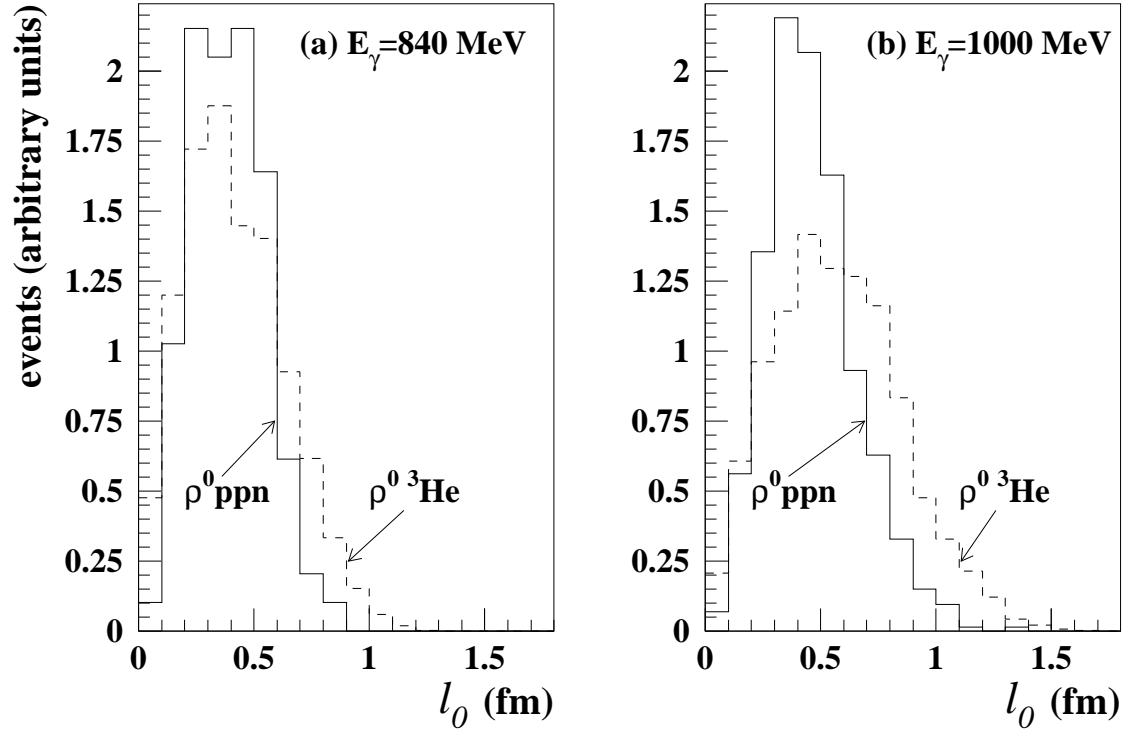


FIG. 13. The mean decay length l_0 distribution, of the $\rho^0 \rightarrow \pi^+\pi^-$ decay, is indicative of the distances probed for vector-meson modifications in this experiment. The l_0 spectra are illustrated for a) $E_\gamma=840$ MeV and b) $E_\gamma=1000$ MeV. The histograms are for MC generated events accepted by the spectrometer in the $\gamma + {}^3\text{He} \rightarrow \rho^0 p(pn)_{sp} \rightarrow \pi^+\pi^- p(pn)_{sp}$ (solid curves) and $\gamma + {}^3\text{He} \rightarrow \rho^0 {}^3\text{He} \rightarrow \pi^+\pi^- {}^3\text{He}$ (dashed curves) reactions, with their integrals normalized to unity. The mean decay length is for the former reaction in the rest frame of the participating proton (the two remaining nucleons being spectators), and for the latter in the rest frame of the ${}^3\text{He}$ nucleus.